Politecnico di Torino

Degree Project in Nuclear Energy Engineering

Second cycle, 30 credits

Kinetic calculations of the bootstrap current with the solver LUKE

LUIGI PERSICO

Kinetic calculations of the bootstrap current with the solver LUKE

LUIGI PERSICO

Date: February 24, 2025

Supervisors: Mathias Hoppe, Joan Decker, Fabio Subba

Considerate la vostra semenza:
fatti non foste a viver come bruti,
ma per seguir virtute e canoscenza.

Inferno, XXVI, 118-120,
Dante Alighieri

Alle passioni,
Alla perseveranza con cui si inseguono,
Alla semplicità con cui si realizzano, ed
A mio nonno Cataldo, che più di tutti ha saputo mostrarmene il significato.

Abstract

In 2023, Earth experienced its warmest year since records began in 1850. This statistic underscores the critical need for sustainable energy solutions. Among the various alternatives, nuclear fusion stands out for its potential to provide clean and abundant energy without the intermittency issues faced by renewable sources or the environmental drawbacks of fossil fuels. However, realizing a nuclear fusion power plant requires overcoming significant technical challenges, particularly in enhancing plasma confinement and stability.

The bootstrap current, a self-generated electric current in plasma, is crucial for maintaining plasma stability and achieving sustained energy output by reducing the dependence on external current drive systems. In this thesis, the LUKE solver, a computational tool designed to calculate the bounce-averaged electron distribution function and its related moments in the low collisionality regime, has been repaired and updated, enabling it to perform accurate calculations of the bootstrap current. This was achieved through a combination of debugging and code optimization, and the obtained results, in different plasma scenarios, are compared with different theoretical models.

Additionally, the thesis examines the effect of the synchrotron reaction force, experienced by particles which are emitting synchrotron radiation, on runaway electrons. This investigation includes the first derivation and implementation of the synchrotron reaction force operator for neoclassical calculations in LUKE. This advancement is crucial for enabling simulations of runaway electrons that consider neoclassical effects, laying the groundwork for potential future calculations of runaway bootstrap currents.

Keywords

Magnetic Confinement Fusion, Bootstrap Current, Runaway Electrons, Synchrotron Reaction Force

Sommario

Nel 2023, la Terra ha sperimentato l'anno più caldo dal 1850, ovvero da quando si hanno a disposizione dati della temperatura terrestre. Questa statistica sottolinea la necessità di soluzioni energetiche sostenibili. Tra le varie alternative, la fusione nucleare si distingue per il suo potenziale di fornire energia pulita e abbondante senza i problemi di intermittenza delle fonti rinnovabili o gli svantaggi ambientali dei combustibili fossili. Tuttavia, realizzare una centrale a fusione nucleare richiede il superamento di significative sfide tecniche, in particolare nel miglioramento del confinamento e della stabilità del plasma.

La corrente di bootstrap, una corrente elettrica autogenerata nel plasma, è cruciale per mantenere la stabilità del plasma, riducendo la dipendenza dai sistemi di alimentazione esterni.

In questa tesi, il solver LUKE, uno strumento computazionale progettato per calcolare la funzione di distribuzione degli elettroni e i suoi relativi momenti in regime di bassa collisionalità, è stato riparato e aggiornato, consentendo nuovamente di eseguire calcoli accurati della corrente di bootstrap. Ciò è stato raggiunto attraverso una combinazione di debugging e ottimizzazione del codice, e i risultati ottenuti, in diversi scenari di plasma, sono confrontati con diversi modelli teorici.

La tesi, inoltre, esamina l'effetto della forza di reazione sincrotronica, la quale agisce su particelle che emettono radiazioni di sincrotrone, sugli elettroni runaway. Questa analisi include la derivazione e l'implementazione dell'operatore della forza di reazione sincrotronica all'interno di LUKE nel caso di calcoli neoclassici. Questo avanzamento è fondamentale per consentire simulazioni di elettroni runaway che considerano effetti neoclassici, gettando le basi per potenziali futuri calcoli delle correnti di bootstrap in presenza di runaways. Questa tesi non solo rivitalizza uno strumento per la ricerca sulla fusione, ma estende anche il quadro teorico per future esplorazioni nel campo.

Parole chiave

Fusione Nucleare, Corrente Bootstrap, Elettroni Runaways, Forza di Reazione Sincrotronica

Acknowledgments

I wish to express my immense gratitude to everyone who contributed to the completion of this academic journey. To *Mathias and Joan*, for their unwavering support. Thank you for guiding me through every step of this path and for pushing me to give my best. You have taught me so much. To *Fabio Subba*, for supervising my work from Politecnico di Torino. To *Andrea, Thomas, and Stefano*, for being my family in Lausanne. Sharing my days with you was one of the best parts of this experience. It will be hard to find someone who plays Exploding Kittens with as much strategy and passion as you do. To *Max, Ewout, Salomon, Sergio,* and all the incredible people I met at *SPC*. Thank you for enriching and lightening my days at the office with a chat, a game of darts, or simply a break together. To *Gaia, Mariateresa, Ivana, and Vincenzo*, my 'centro di gravità permanente'. No matter how far I may orbit, every achievement of mine is also yours; I am lucky to have you in my life. To *Matteo*, and your incredible energy. You are always there, ready for a conversation — whether it's about wave physics, One Piece, the next interview, or some absurd adventure we've been through. With you, any problem can be tackled with surprising ease. To *Sara*, the most beautiful thing this master's journey has given me. Thank you for always being ready to listen and support me, even when I make it hard to do. May this be just the first of many milestones together. Te quiero. To *my brother Carmine and my sister Valentina*, my lifelong playmates and companions. You are my number one fans, my most sincere critics, and with you, everything feels effortless. Many have traveled by plane, but few know the thrill of a (true) 'atterraggio'. To *Mom and Dad*, the foundation upon which my life has been built. Thank you because, even though you never had the chance to pursue a university career, you always try to understand and support my choices. I wouldn't be here at the end of this journey if it weren't for the trust and love you give me every day. To *my grandfather Cataldo, my grandmother Luisa, and my entire family*, who have always been my 'Vivaldi's Spring' playing in the background. Only by growing up and living far away, have I truly understood how important you are to me. To *Stockholm*, to the *Keglevich fanbase*, and to all the amazing people I have met here. To *Turin*, the city that has seen me grow the most, to *Collegio Einaudi* and everyone who shared it with me, to *Energetica is the way* and the *Bimbe di Danielone*; I will carry the years spent here as some of the most beautiful of my life.

Ringraziamenti

Desidero esprimere la mia immensa gratitudine a tutti coloro che hanno contribuito al completamento di questo percorso accademico. A *Mathias e Joan* con il loro immancabile supporto. Grazie per avermi guidato in ogni step di questo percorso e per avermi spinto a dare il meglio. Mi avete insegnato tanto. A *Fabio Subba* per essere stato il mio supervisor lato Politecnico di Torino. Ad *Andrea, Thomas e Stefano*, per essere stati la mia famiglia a Losanna. Condividere con voi le mie giornate è stata una della parti più belle di quest'esperienza. Sarà difficile incontrare qualcuno in grado di giocare ad Exploding Kittens con tanta strategia e passione. A *Max, Ewout, Salomon, Sergio* e a tutte le incredibili persone incontrate ad *SPC*. Grazie per aver arricchito e alleggerito le mie giornate in ufficio con una chiacchierata, una partita a freccette o una semplice pausa in compagnia. A *Gaia, Mariateresa, Ivana e Vincenzo*, il mio centro di gravità permanente. Per quanto io possa orbitare in lontananza, ogni mio traguardo è anche vostro; sono fortunato ad avervi nella mia vita. A *Matteo*, ed alla tua incredibile energia. Sei sempre lì, pronto ad una chiacchierata, che sia sulla fisica delle onde, su One Piece, sul prossimo colloquio, o su qualche avventura assurda che ci è capitata. Con te è possibile affrontare qualsiasi problema con una leggerezza sorprendente. A *Sara*, la cosa più bella che questo percorso magistrale mi abbia lasciato. Grazie per essere sempre pronta ad ascoltarmi e sostenermi, anche quando lo rendo difficile. Che questo sia solo il primo di tanti traguardi insieme. Te quiero. A *mio fratello Carmine e mia sorella Valentina*, i miei compagni di giochi e di vita. Siete i miei fan numero uno, i miei critici più sinceri, con voi la naturalezza regna sovrana. Molti hanno viaggiato in aereo, ma pochi conoscono il brio di un (vero) atterraggio. A *mamma e papà*, le fondamenta su cui la mia vita è stata costruita. Grazie perchè, pur non avendo mai potuto intraprendere una carriera universitaria, cercate sempre di capire ed appoggiare le mie scelte. Non sarei qui alla conclusione di questo percorso se non fosse per la fiducia e l'amore che mi donate ogni giorno. A *mio nonno Cataldo, mia nonna Luisa e a tutta la mia famiglia*, che da sempre costituiscono la mia primavera di Vivaldi in sottofondo. Solo crescendo e vivendo lontano ho capito davvero quanto importanti siate per me. A *Stoccolma*, ai *Keglevich fanbase* e a tutte le fantastiche persone qui conosciute. A *Torino*, la città che più mi ha visto crescere, al *Collegio Einaudi* e tutti coloro che con me l'hanno vissuto, agli *Energetica is the way* e alle *Bimbe di Danielone*; porterò gli anni vissuti qui come tra i più belli della mia vita.

Contents

List of Figures

List of Tables

Chapter 1

Introduction

"The year 2023 was the warmest year since global records began in 1850 at 1.18°C (2.12°F) above the 20th century average of 13.9°C" [1]. While some might think that such a single-year anomaly could merely be a result of natural climate fluctuations, the long-term trend of the past 173 years, as shown in Figure 1.1, strongly suggests otherwise. It is evident that human activities are impacting Earth's climate. Climate change is no longer just a future risk that depends on environmental care, it is a present reality.

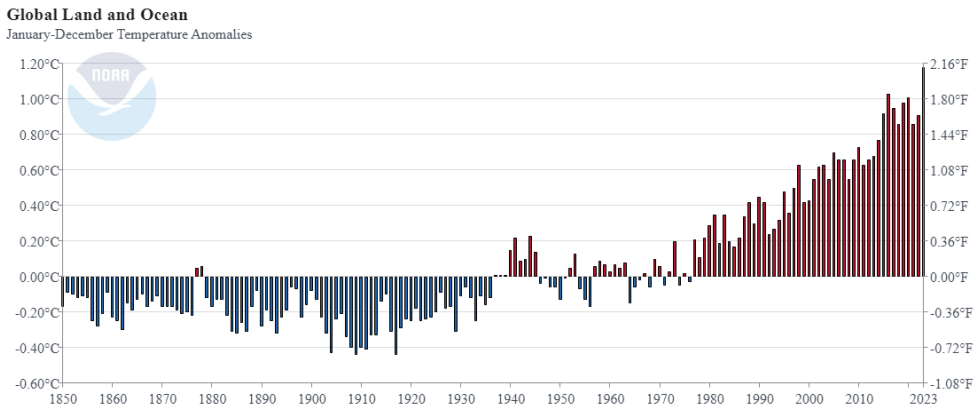

Figure 1.1: Global land and ocean average temperature anomalies, from 1850 to 2023 [1].

The main driver of extreme temperature increases is the rise in greenhouse gas emissions, which have been growing since the first Industrial Revolution in the 19th century. Among the most impactful sectors for greenhouse gas emissions is energy production. Modern society requires vast amounts of

energy to function, and one of the biggest challenges today is to generate this energy in an affordable and environmentally friendly way. While renewable energy sources produce minimal carbon emissions, they face a significant drawback: intermittency. Renewable energy cannot always meet demand when needed, and current energy storage solutions still have high environmental impacts and costs.

Nuclear fission, on the other hand, offers steady energy production with minimal land use and one of the lowest greenhouse gas emissions. However, nuclear fission presents challenges of its own, such as radioactive waste, limited public acceptance, and the unequal distribution of uranium resources worldwide. It might seem that a perfect energy source does not exist, but there is one that has always been in view, whether from the Sun during the day or from the stars at night: nuclear fusion. Fusion is the most attractive solution, though commercializing it poses some of the most complex physics and engineering challenges humanity has ever faced.

Achieving fusion on Earth requires temperatures around 200 million kelvin to overcome the electrostatic repulsion between atomic nuclei. At these extreme temperatures, matter becomes an ionized gas known as plasma, which must be carefully confined. The most promising approach is magnetic confinement, using strong magnetic fields arranged in a closed, toroidal shape. Two leading technologies for this are the tokamak and the stellarator, both under active study, with the tokamak being the one with the most years of experience and with the best achieved performance. The main difference between them is how the poloidal field, shown by the circulating arrows in Figure 1.2, is generated: while in the stellaretor it is done with 3D-shaped coils, in a tokamak a strong current is induced in the plasma using a central solenoid, shown in blue in Figure 1.2.

In tokamaks, understanding plasma particle behavior, especially electrons, is crucial for maintaining stability and confinement. Instabilities can sometimes disrupt this confinement, leading to abrupt temperature drops; these events, known as disruptions, increase plasma resistivity and generate high electric fields. When these fields exceed critical values, they can trigger the formation of runaway electrons. These electrons, initially part of the thermal plasma, experience rapid acceleration due to the intense electric fields created during disruptions. As they accelerate to relativistic speeds, they become capable of causing severe damage to reactor walls upon impact, highlighting the necessity of understanding their generation and behavior to prevent and manage disruptions effectively.

The complexity and non-linearity of plasma physics often preclude

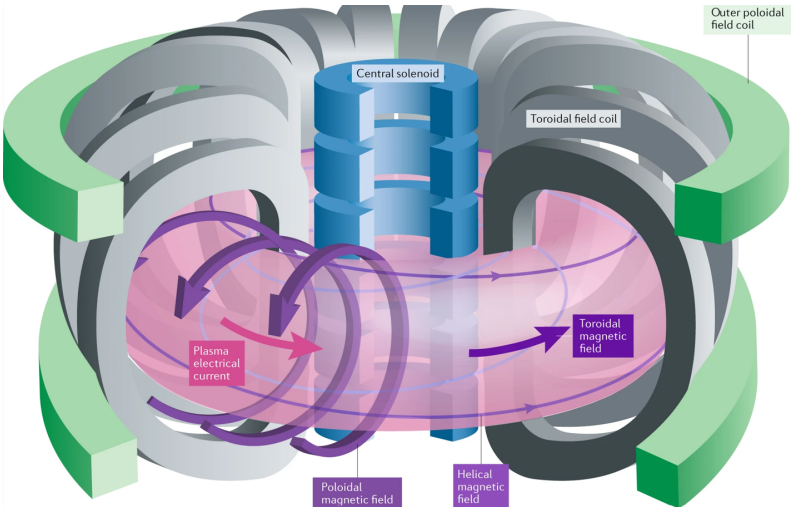

Figure 1.2: Tokamak main structure [2]. In grey the toroidal fields coils, in blue the central solenoid to induce the current in the plasma for the poloidal field, and in green the vertical field coils.

general analytic solutions, requiring various models and computational tools. Among these, the neoclassical phenomenon of the bootstrap current, a self-generated, non-inductive current arising from particle pressure and temperature gradients, plays a vital role in enhancing plasma stability and reducing dependence on external current drive [3]. High bootstrap current fractions suggest a potential to eliminate external current sources post-startup when reaching good plasma scenarios. However, experimentally isolating different current contributions to measure the bootstrap current is highly challenging, making theoretical kinetic models critical for accurate predictions.

The electron behavior in tokamaks is governed by the Fokker-Planck equation. Due to its high computational demands, simplifications are made by averaging over faster timescales, reducing dimensionality. The LUKE code, a tool for approximating the Fokker-Planck equation, handles calculations at both zeroth and first orders of orbit width. While in zeroth order, particles exactly follow magnetic field lines, the first order includes drift effects from magnetic field curvature and gradients, crucial for understanding neoclassical effects like the bootstrap current. Unfortunately, the first order mode of LUKE has been rendered inoperative in recent years, preventing bootstrap current calculations.

Furthermore, when electrons turn into runaways, they accelerate until reaching relativistic speeds and start emitting synchrotron radiation. As a

consequence of the radiation, the electrons experience in return a sort of drag force, known as the synchrotron reaction or Abram-Lorentz-Dirac (ALD) force. This force is crucial in preventing infinite acceleration, allowing electrons to stabilize at a momentum limit. Currently, LUKE includes this force only in its zeroth order approximation, thereby preventing complete neoclassical runaway electron calculations.

This thesis aims to deepen the understanding of LUKE's underlying theory, restore first order bootstrap current calculations, and theoretically derive and implement the ALD force in the neoclassical context within the code.

In Chapter 2 the theoretical foundations on which the code is based, the theory of the synchrotron reaction force and the theory of the bootstrap current are presented. Chapter 3 explains the methods used for this work, starting with LUKE's grid and outputs, and then focusing on different choices of bootstrap current models. In Chapter 4, the results are presented: firstly the bootstrap current computed through simulations in LUKE is compared to the bootstrap current models in different plasma scenarios; secondly, the effect that synchrotron reaction force has on runaway electrons is discussed. Finally, Chapter 5 provides conclusions and outlines future work.

Chapter 2

Background

2.1 Particle motion in tokamaks

A tokamak is a toroidal device which confines charged particles using strong magnetic fields. Generally speaking, a charged particle in an electromagnetic field is subject to the Lorentz force

$$\boldsymbol{F} = q(\boldsymbol{E} + \boldsymbol{v} \times \boldsymbol{B}), \tag{2.1}$$

where q is the particle charge, $\boldsymbol{v}$ is its velocity, and $\boldsymbol{E}$ and $\boldsymbol{B}$ are the electric and magnetic fields. The velocity $\boldsymbol{v}$ can be decomposed into

$$\boldsymbol{v} = v_{\parallel}\hat{\boldsymbol{e}}_{\parallel} + v_{\perp}\hat{\boldsymbol{e}}_{\perp}, \tag{2.2}$$

where the components are respectively parallel and perpendicular to $\boldsymbol{B}$. Performing the cross product in Eq. (2.1)

$$\boldsymbol{F} = q\left[\boldsymbol{E} + (v_{\parallel}\hat{\boldsymbol{e}}_{\parallel} + v_{\perp}\hat{\boldsymbol{e}}_{\perp}) \times B\hat{\boldsymbol{e}}_{\parallel}\right] = q\left[\boldsymbol{E} + v_{\perp}B(\hat{\boldsymbol{e}}_{\perp} \times \hat{\boldsymbol{e}}_{\parallel})\right], \tag{2.3}$$

which means that, without considering the effect of the electric field, $v_{\parallel}$ would just let the particle move along $\hat{\boldsymbol{e}}_{\parallel}$, while $v_{\perp}$ would generate the Lorentz force and constrain the particle to move around the magnetic field lines with a circular motion of frequency $\Omega = |q|B/(\gamma m)$, and radius $r_L = v_{\perp}/\Omega$, with m the particle rest mass, $\gamma = 1/\sqrt{1 - \boldsymbol{v}^2/c^2}$ the relativistic factor, and c the light speed. Therefore, the sum of the two contributions consists in a helical trajectory around the magnetic field lines, as is shown in Figure 2.1.

The magnetic field in a tokamak is not uniform, rather its magnitude decreases with the distance from the tokamak symmetry axis. Particles

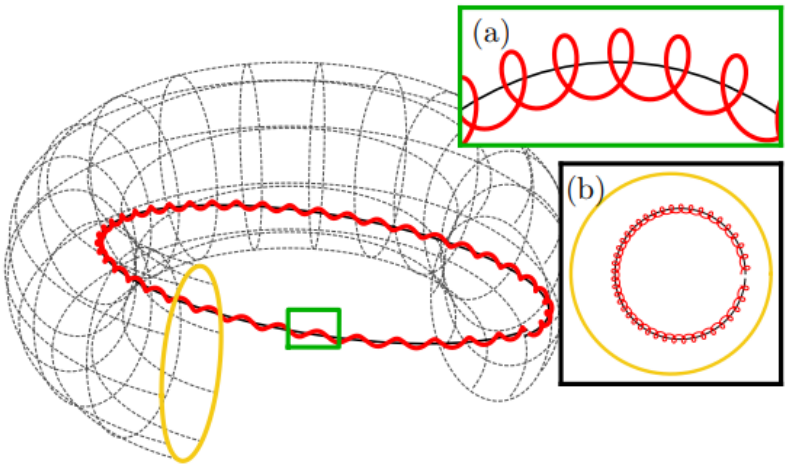

Figure 2.1: How charged particles move in a tokamak magnetic field. Their helical orbits around field lines are highlighted in (a), while their orbit projected onto a poloidal plane is shown in (b) [4].

circling around the magnetic field lines are therefore experiencing a varying force during their gyro-motion. This means that the radius of the orbit is changing slightly and, depending on the direction of the rotation, i.e. on the charge sign, the particle will slowly move upwards or downwards in the poloidal plane. The drift velocity due to this phenomenon can be expressed as [5]

$$\boldsymbol{v}_{D,\nabla B} = \pm \frac{v_\perp^2}{2\Omega} \frac{\boldsymbol{B} \times \boldsymbol{\nabla} B}{B^2}. \tag{2.4}$$

Magnetic field lines in a tokamak are also bent, which means that the particles, while moving along the field lines, experience a centrifugal force, which makes them drift with a velocity in the direction of $\boldsymbol{v}_{\boldsymbol{D},\nabla \boldsymbol{B}}$ [5]:

$$\boldsymbol{v}_{D,\text{curv}} = \pm \frac{v_\parallel^2}{\Omega} \frac{\boldsymbol{B} \times \boldsymbol{\nabla} B}{B^2}. \tag{2.5}$$

It is for this reason that a purely toroidal magnetic field $\boldsymbol{B}_T$ would lead to a net charge separation, and loss of confinement. Therefore, a poloidal field $\boldsymbol{B}_P$ is needed to cancel out the drifts particles are subject to while following their paths. Adding such a poloidal component to the magnetic field, generated by a strong current induced in the plasma, the total magnetic field $\boldsymbol{B}$ takes the general form

$$\boldsymbol{B} = \boldsymbol{B}_T + \boldsymbol{B}_P, \tag{2.6}$$

which means that the magnetic field lines are twisted around the toroidal direction. The number of toroidal transits completed for every poloidal one, is defined as the safety factor $\bar{q}$, which is in reality dependent on the minor radius, and it should be major than one at all the points in the plasma for stability reasons.

In a plasma scattering events are mainly inelastic, i.e. the kinetic energy W_k of particles is not conserved during collisions. Making the assumption of a plasma sufficiently non-collisional, hence with a high collision time scale, the kinetic energy is conserved at time scales smaller than the collision time scale. In the non-relativistic limit this can be written as

$$W_k = \frac{m}{2}(v_\parallel^2 + v_\perp^2) = \text{const.} \tag{2.7}$$

It can be demonstrated that the magnetic moment $\mu \equiv mv_\perp^2/(2B)$ of a particle is an adiabatic invariant, therefore it can be considered as a constant of motion if the magnetic field is not rapidly changing. Using the magnetic moment, the conservation of the kinetic energy can written as

$$W_k = \frac{mv_\parallel^2}{2} + \mu B = \text{const.} \tag{2.8}$$

If a particle has an initial velocity $\boldsymbol{v}_0 = v_{\parallel,0}\hat{\boldsymbol{e}}_\parallel + v_{\perp,0}\hat{\boldsymbol{e}}_\perp$, when the magnetic field strength is B_0, the conservation of μ and Eq. (2.8) would lead to $v_\parallel = 0$ at the point highest field along the orbit, if the condition

$$\frac{v_{\perp,0}^2}{v_{\perp,0}^2 + v_{\parallel,0}^2} \geq \frac{B_0}{B_{\text{max}}}, \tag{2.9}$$

is satisfied, with B_{max} the highest field the particle is experiencing along the orbit. When this happens, the parallel velocity is forced to change sign, i.e. the particle bounces back on a trajectory slightly different from the previous one due to drift effects. In this case the orbit is referred to as a "trapped orbit", since particles satisfying Eq. (2.9) will keep bouncing back and forth between two different poloidal angles. As the orbit shape resembles a banana, it is usually called "banana orbit", and its width "banana width". In Figure 2.2 both orbits are shown.

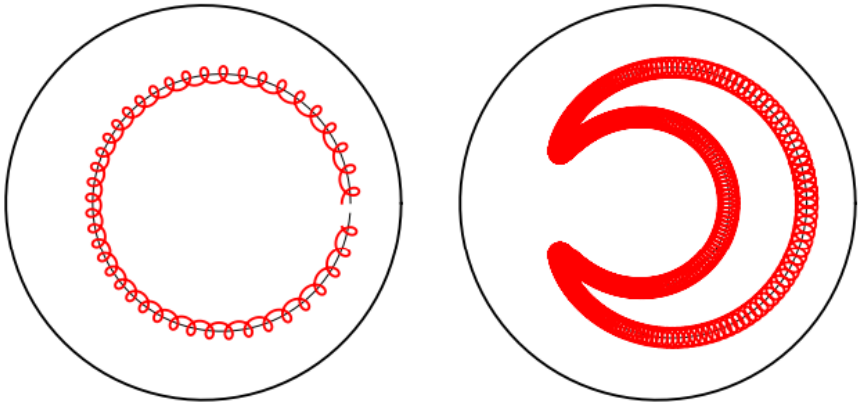

Figure 2.2: Particle orbits projected onto a poloidal cross section. On the left a passing orbit; on the right a trapped or banana orbit [4].

2.2 Kinetic theory of electrons

To fully describe the evolution of a large number of particles, with position $\boldsymbol{r}$ and momentum $\boldsymbol{p}$, over time t, the so called phase space* density $f(\boldsymbol{r}, \boldsymbol{p}, t)$ is often used, which is related to the total number of particles as

$$N = \int \mathrm{d}\boldsymbol{r} \int \mathrm{d}\boldsymbol{p}\, f(\boldsymbol{r}, \boldsymbol{p}, t). \tag{2.10}$$

In this specific case, the particles of interest are electrons in a magnetized plasma, with an associated phase space density $f_e(\boldsymbol{r}, \boldsymbol{p}, t)$. Its evolution is governed by the Boltzmann equation

$$\frac{\partial f_e(\boldsymbol{r}, \boldsymbol{p}, t)}{\partial t} + \{f_e(\boldsymbol{r}, \boldsymbol{p}, t), \mathcal{H}_e\} = \left.\frac{\partial f_e(\boldsymbol{r}, \boldsymbol{p}, t)}{\partial t}\right|_{\mathcal{C}}, \tag{2.11}$$

where $\mathcal{H}_e$ is the Hamiltonian of the system, $\{\cdot, \cdot\}$ are the Poisson brackets, and

$$\left.\frac{\partial f_e(\boldsymbol{r}, \boldsymbol{p}, t)}{\partial t}\right|_{\mathcal{C}} \equiv \mathcal{C}(f_e) \tag{2.12}$$

is the collision operator. Omitting the explicit dependencies, expressing $\mathcal{H}_e$, and taking into account just the Lorentz force, Eq. (2.11) can be then rewritten

*Given an n-dimensional Euclidean space, the associated phase space is a $2n$-dimensional space with variables $\boldsymbol{r}$ and $\boldsymbol{p}$. In the case of interest $n = 3$.

as

$$\frac{\partial f_e}{\partial t} + \boldsymbol{v} \cdot \boldsymbol{\nabla}_{\boldsymbol{r}} f_e + q(\boldsymbol{E} + \boldsymbol{v} \times \boldsymbol{B}) \cdot \boldsymbol{\nabla}_{\boldsymbol{p}} f_e = \mathcal{C}(f_e). \tag{2.13}$$

2.3 Coordinate system

Since the electrons of interest are confined inside a tokamak, an appropriate coordinate system must be introduced to best describe their dynamics, to take advantage of the symmetry, and to reduce the problem dimensionality.

2.3.1 Configuration space

There are three main coordinate systems used to describe the electron configuration space in LUKE:

- The coordinate system (R, Z, ϕ), where R is the distance from the torus axis, Z is the distance along the axis, and ϕ is the toroidal angle. This system is the most general one, and it is shown in Figure 2.3a.
- The coordinate system (r, θ, ϕ), where r is the distance from the toroidal axis (R_p, Z_p) and θ is the poloidal angle.
- The coordinate system (ψ, θ, ϕ), shown in Figure 2.3b, where ψ is the poloidal magnetic flux*. As an alternative to this system (ψ, s, ϕ) can be used, where s is the coordinate parallel to the flux surface; it expresses the length along the poloidal magnetic field lines.

2.3.2 Momentum space

For momentum space there are two main options, both highlighted in Figure 2.4:

- Cylindrical coordinate system $(p_\parallel, p_\perp, \varphi)$, where $p_\parallel$ is the momentum component along the magnetic field lines, $p_\perp$ is the perpendicular one, and φ is the gyro-angle.
- Spherical coordinate system (p, ξ, φ), where $p = |\boldsymbol{p}|$ and $\xi = p_\parallel / p$. This system is better suited to describe particle collisions.

*In the approximation of particles exactly following magnetic field lines, i.e. considering the drift velocities equal zero, ψ is a constant of motion.

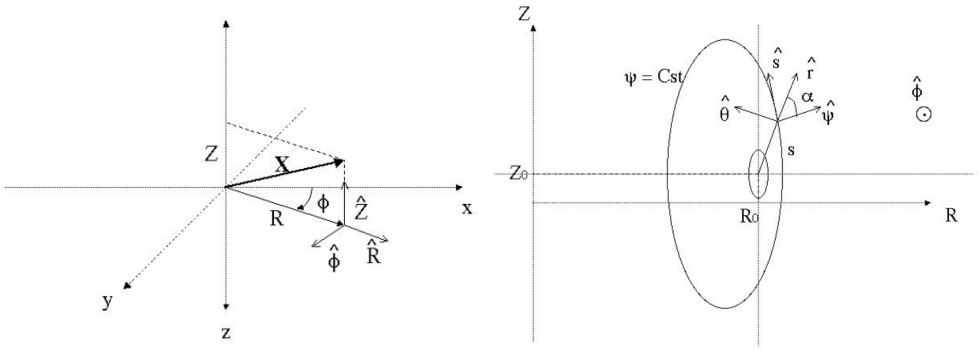

(a) The coordinate system (R, Z, ϕ) (b) The coordinate system (ψ, θ, ϕ)

Figure 2.3: Coordinate systems for the configuration space [6].

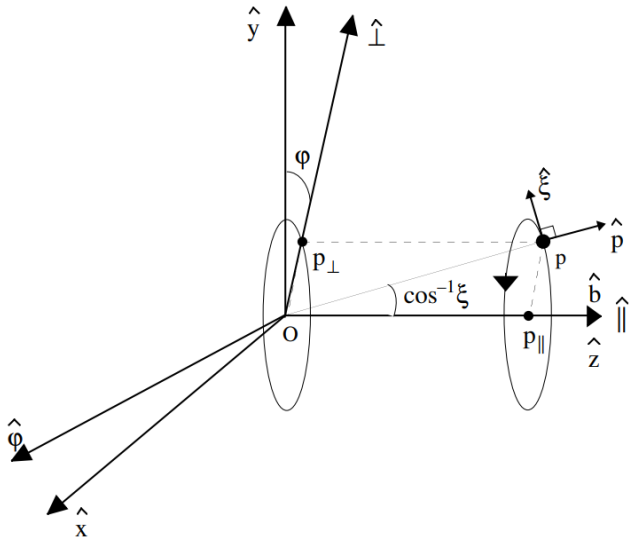

Figure 2.4: Coordinate systems for the momentum space [6]. Both the cylindrical and the spherical system are shown.

However, as explained in Section 2.1, the conservation of the magnetic moment leads to a continuous variation of the momentum components, and specifically of the cosine of the pitch angle ξ. It is therefore more convenient to replace this coordinate with ξ_0, which in this case corresponds to the pitch value at the minimum magnetic field point along that specific orbit. Once the value of ξ_0 has been specified, it is possible to get the pitch at every point of

the orbit as

$$\xi = \pm\sqrt{1 - \Psi(1 - \xi_0^2)}, \tag{2.14}$$

where $\Psi = \Psi(\psi, \theta) \equiv B(\psi, \theta)/B_0(\psi)$, and $B_0 = B_{min}$. For convenience, the trapped condition, expressed in Eq. (2.9), is usually rewritten as

$$|\xi_0| \leq |\xi_{0T}|, \tag{2.15}$$

with

$$\xi_{0T}^2 = 1 - \frac{B_0}{B_{max}}. \tag{2.16}$$

Using the coordinate system (p, ξ_0, φ) instead of (p, ξ, φ) is useful when integrating over a poloidal transit, since ξ_0 is in that case a constant. Differentiating Eq. (2.14) it is possible to obtain that

$$\xi \mathrm{d}\xi = \Psi \xi_0 \mathrm{d}\xi_0. \tag{2.17}$$

2.4 Wave-, gyro- and bounce-averaging

2.4.1 Time scales in tokamaks

The plasma phenomena inside a tokamak are characterised by many different time scales, which can be ordered according to their magnitudes. The fastest phenomenon is typically the gyro-motion and the electromagnetic wave oscillation, with characteristic times $\tau_\Omega = \Omega^{-1} = \gamma m/qB$ and τ_w respectively. The transit or bounce time scale τ_b, which is the time required for a particle to complete a poloidal transit (either completing $\bar{q}$ toroidal transits, or bouncing back), can be generally computed as

$$\tau_\mathrm{b} = \oint_\Gamma \frac{\mathrm{d}s}{|v_s|}, \tag{2.18}$$

where s is the distance along a poloidal magnetic field line, Γ is the full particle orbit, and $v_s = v_\parallel(\hat{\boldsymbol{e}}_\parallel \cdot \hat{\boldsymbol{s}})$ is the velocity along the poloidal field lines. Finally, other time scales of interest are the collision time scale τ_c, the electric field acceleration time scale τ_acc and the radiation energy loss time scale τ_rad. In the case of low-collisionality plasmas, they can all be ordered as according to [4]

$$\tau_\Omega, \tau_\mathrm{w} \ll \tau_\mathrm{b} \ll \tau_\mathrm{c}, \tau_\mathrm{acc}, \tau_\mathrm{rad}. \tag{2.19}$$

2.4.2 Wave-averaging

The fields $\boldsymbol{E}(\boldsymbol{r},t)$ and $\boldsymbol{B}(\boldsymbol{r},t)$ in Eq. (2.13) can be written as the sum of stationary background macroscopic components $\bar{\boldsymbol{E}}(\boldsymbol{r})$ and $\bar{\boldsymbol{B}}(\boldsymbol{r})$, and time dependent components, coming from the externally injected waves, which can be expressed using Fourier transforms:

$$\boldsymbol{E}(\boldsymbol{r},t) = \bar{\boldsymbol{E}}(\boldsymbol{r}) + \int \tilde{\boldsymbol{E}}_{\boldsymbol{k}} \mathrm{e}^{i(\boldsymbol{k}\cdot\boldsymbol{r}-\omega t)} \mathrm{d}\boldsymbol{k}, \tag{2.20}$$

$$\boldsymbol{B}(\boldsymbol{r},t) = \bar{\boldsymbol{B}}(\boldsymbol{r}) + \int \tilde{\boldsymbol{B}}_{\boldsymbol{k}} \mathrm{e}^{i(\boldsymbol{k}\cdot\boldsymbol{r}-\omega t)} \mathrm{d}\boldsymbol{k}, \tag{2.21}$$

where $\boldsymbol{k}$ and ω are respectively the wave vector and the angular frequency. Performing a time-averaging of Eq. (2.13) on the wave time scale [6]:

$$\frac{\partial \bar{f}_e}{\partial t} + \boldsymbol{v}\cdot\boldsymbol{\nabla}_{\boldsymbol{r}}\bar{f}_e + q(\bar{\boldsymbol{E}} + \boldsymbol{v}\times\bar{\boldsymbol{B}})\cdot\boldsymbol{\nabla}_{\boldsymbol{p}}\bar{f}_e = \mathcal{C}(\bar{f}_e) + \mathcal{Q}(\bar{f}_e), \tag{2.22}$$

where $\bar{f}_e = \int_0^{2\pi/\omega} f_e \mathrm{d}t$, and

$$\mathcal{Q}(\bar{f}_e) = -\int_0^{2\pi/\omega} \sum_{\boldsymbol{k}} [q(\tilde{\boldsymbol{E}}_{\boldsymbol{k}} + \boldsymbol{v}\times\tilde{\boldsymbol{B}}_{\boldsymbol{k}})\cdot\boldsymbol{\nabla}_{\boldsymbol{p}} f_e]\mathrm{d}t \tag{2.23}$$

is the quasilinear operator, which described how the plasma reacts to the electromagnetic wave fields.

2.4.3 Gyro-averaging

Assuming conditions such that the ordering (2.19) is satisfied, it is possible to expand the phase space density $\bar{f}_e$ with respect to the small parameter $\delta_\Omega \sim \tau_\Omega/\tau_c$:

$$\bar{f}_e = \bar{f}_{e,0} + \bar{f}_{e,1} + O(\delta_\Omega^2). \tag{2.24}$$

From the zeroth order form of Eq. (2.22), it is found that $\bar{f}_{e,0}$ is independent of the gyro-angle φ, while the first order equation reads

$$\frac{\partial \bar{f}_{e,0}}{\partial t} + \boldsymbol{v}\cdot\boldsymbol{\nabla}_{\boldsymbol{r}}\bar{f}_{e,0} + q(\bar{\boldsymbol{E}} + \boldsymbol{v}\times\bar{\boldsymbol{B}})\cdot\boldsymbol{\nabla}_{\boldsymbol{p}}\bar{f}_{e,1} = \mathcal{C}(\bar{f}_{e,0}) + \mathcal{Q}(\bar{f}_{e,0}). \tag{2.25}$$

Eq. (2.25) can be then averaged along the gyro-motion, to obtain the so-called *drift-kinetic equation*:

$$\frac{\partial \tilde{f}_{e,0}}{\partial t} + \boldsymbol{v}_{GC} \cdot \boldsymbol{\nabla}_{\boldsymbol{r}} \tilde{f}_{e,0} = \mathcal{C}(\tilde{f}_{e,0}) + \mathcal{Q}(\tilde{f}_{e,0}) + \mathcal{E}(\tilde{f}_{e,0}), \tag{2.26}$$

where

$$\tilde{f}_{e,0} = \int_0^{2\pi} \bar{f}_{e,0} \, \mathrm{d}\varphi \tag{2.27}$$

is the gyro-averaged distribution,

$$\boldsymbol{v}_{GC} = \int_0^{2\pi} \boldsymbol{v} \, \mathrm{d}\varphi = v_{\parallel} \hat{\boldsymbol{e}}_{\parallel} + \boldsymbol{v}_D \tag{2.28}$$

is the guiding center velocity, with $\boldsymbol{v_D}$ the drift component, and

$$\mathcal{E}(\tilde{f}_{e,0}) = -q\bar{E}_{\parallel} \frac{\partial \tilde{f}_{e,0}}{\partial p_{\parallel}} \tag{2.29}$$

is the electric field operator. It is interesting to note that, if expanding the magnetic field considering the small perturbations along the gyro-radius, Eq. (2.25) takes the form

$$\frac{\partial \bar{f}_{e,0}}{\partial t} + \boldsymbol{v} \cdot \boldsymbol{\nabla}_{\boldsymbol{r}} \bar{f}_{e,0} + q \left(\bar{\boldsymbol{E}} + \boldsymbol{v} \times \bar{\boldsymbol{B}} - \frac{\mu}{q} \boldsymbol{\nabla}_{\boldsymbol{r}} B \right) \cdot \boldsymbol{\nabla}_{\boldsymbol{p}} \bar{f}_{e,1} = \mathcal{C}(\bar{f}_{e,0}) + \mathcal{Q}(\bar{f}_{e,0}), \tag{2.30}$$

and, when gyro-averaging, a new operator, $\mathcal{M}(\tilde{f}_{e,0})$, comes out. In this case Eq. (2.26) reads

$$\frac{\partial \tilde{f}_{e,0}}{\partial t} + \boldsymbol{v}_{GC} \cdot \boldsymbol{\nabla}_{\boldsymbol{r}} \tilde{f}_{e,0} = \mathcal{C}(\tilde{f}_{e,0}) + \mathcal{Q}(\tilde{f}_{e,0}) + \mathcal{E}(\tilde{f}_{e,0}) + \mathcal{M}(\tilde{f}_{e,0}), \tag{2.31}$$

where

$$\mathcal{M}(\tilde{f}_{e,0}) = \mu(\hat{\boldsymbol{e}}_{\parallel} \cdot \boldsymbol{\nabla}\theta) \frac{\partial B}{\partial \theta} \frac{\partial \tilde{f}_{e,0}}{\partial p_{\parallel}} \tag{2.32}$$

is the magnetic moment operator. Both $\mathcal{E}(\tilde{f}_{e,0})$ and $\mathcal{M}(\tilde{f}_{e,0})$ are affecting the distribution function along the parallel momentum, but while the first operator is coming from the effect of the electric field in that direction, the second operator arises from the conservation of the magnetic moment, and it is zero in the case of a purely toroidal magnetic field. In $\mathcal{M}(\tilde{f}_{e,0})$, only the variation of the poloidal magnetic field enters, since the magnetic field is symmetric in the

toroidal direction (i.e. the toroidal derivative is zero). The magnetic moment operator is smaller in magnitude than the other operators, and when bounce-averaging its net effect is zero. For these reasons it will not be considered from now on.

Finally, considering a distribution function constant in time, i.e. $\partial \tilde{f}_{e,0}/\partial t = 0$, and expanding the velocity $\boldsymbol{v}_{GC}$, Eq. (2.26) becomes

$$v_{\parallel}\hat{\boldsymbol{e}}_{\parallel} \cdot \boldsymbol{\nabla}_{\boldsymbol{r}} \tilde{f}_{e,0} + \boldsymbol{v}_D \cdot \boldsymbol{\nabla}_{\boldsymbol{r}} \tilde{f}_{e,0} = \mathcal{C}(\tilde{f}_{e,0}) + \mathcal{Q}(\tilde{f}_{e,0}) + \mathcal{E}(\tilde{f}_{e,0}), \tag{2.33}$$

and, rearranging the terms, it is possible to get

$$v_s \frac{\tilde{f}_{e,0}}{\partial s} + (\boldsymbol{v_D} \cdot \boldsymbol{\nabla}\psi)\frac{\tilde{f}_{e,0}}{\partial \psi} = \mathcal{C}(\tilde{f}_{e,0}) + \mathcal{Q}(\tilde{f}_{e,0}) + \mathcal{E}(\tilde{f}_{e,0}). \tag{2.34}$$

2.4.4 Drift evaluation

As explained in Section 2.1, the drift velocity $\boldsymbol{v}_D$ of a charged particle in a tokamak magnetic field $\boldsymbol{B}$, with a certain curvature and gradient, can be expressed as

$$\boldsymbol{v}_D = \frac{1}{\Omega_e}\left(v_{\parallel}^2 + \frac{v_{\perp}^2}{2}\right)\frac{\boldsymbol{B} \times \boldsymbol{\nabla} B}{B^2}. \tag{2.35}$$

Rearranging the terms, and using the general form of a magnetic field in a toroidal axisymmetric geometry

$$\boldsymbol{B} = I(\psi)\boldsymbol{\nabla}\phi + \boldsymbol{\nabla}\psi \times \boldsymbol{\nabla}\phi, \tag{2.36}$$

such that $B_T = |I(\psi)||\boldsymbol{\nabla}\phi|$ and $B_P = |\boldsymbol{\nabla}\psi||\boldsymbol{\nabla}\phi|$ are the toroidal and poloidal components of the magnetic field, it is possible to rewrite the component along $\boldsymbol{\nabla}\psi$ of the drift velocity as [6]

$$\boldsymbol{v}_D \cdot \boldsymbol{\nabla}\psi = \frac{v_{\parallel}}{\Omega_e} I(\psi)\boldsymbol{B} \cdot \boldsymbol{\nabla}\left(\frac{v_{\parallel}}{B}\right). \tag{2.37}$$

Knowing the drift component of the velocity across the magnetic surfaces, the time scale τ_d associated to this effect can be determined as

$$\tau_{\mathrm{d}}(\psi') = \int_0^{\psi'} \frac{\mathrm{d}\psi}{\boldsymbol{v}_D \cdot \boldsymbol{\nabla}\psi}. \tag{2.38}$$

In order to understand how much relevance the drift has compared to the motion along the magnetic field lines, a small drift parameter δ_d can be defined

as

$$\delta_d \equiv \frac{\tau_b}{\tau_d(\psi_a)} \sim \frac{r_L}{a}, \tag{2.39}$$

where τ_b is the transit or bounce time defined in Eq. (2.18), r_L is the Larmor radius, a is the plasma minor radius, and ψ_a is the value of ψ at the plasma boundary.

2.4.4.1 Small drift limit

Under the assumption of small drifts, $\delta_d \ll 1$, the distribution function $\tilde{f}_{e,0}$ can be expanded again, this time with respect to the small drift parameter δ_d, in

$$\tilde{f}_{e,0} = \tilde{f}_{e,00} + \tilde{f}_{e,01} + O(\delta_d^2). \tag{2.40}$$

Starting from Eq. (2.34), the zeroth order steady-state drift-kinetic equation, also known as the steady-state zeroth order Fokker-Plank equation, is

$$v_s \frac{\partial \tilde{f}_{e,00}}{\partial s} = \mathcal{C}(\tilde{f}_{e,00}) + \mathcal{Q}(\tilde{f}_{e,00}) + \mathcal{E}(\tilde{f}_{e,00}), \tag{2.41}$$

while, when considering the first order, the steady-state drift-kinetic equation is obtained:

$$v_s \frac{\partial \tilde{f}_{e,01}}{\partial s} + (\boldsymbol{v_D} \cdot \boldsymbol{\nabla}\psi) \frac{\partial \tilde{f}_{e,00}}{\partial \psi} = \mathcal{C}(\tilde{f}_{e,01}) + \mathcal{Q}(\tilde{f}_{e,01}) + \mathcal{E}(\tilde{f}_{e,01}). \tag{2.42}$$

It is important to note that, in Eq. (2.41), the effects related to the electrons drift motion are not taken into account. Therefore, when electrons are trapped into a banana orbit, they are moving back and forth on the same curve, while Eq. (2.42) also describes how the banana orbit gets its width.

2.4.5 Bounce-averaging

Prior to continuing, since the notation of the distribution function has become quite heavy, it is beneficial to simplify it. Before doing so, a recap of the operations done is in order. First of all, a general electron distribution function, dependent on time and phase space coordinates, has been introduced $f_e = f_e(\boldsymbol{x}, \boldsymbol{p}, t)$. Electrons moving in the plasma are subject to the Lorentz force, and, since part of it is generated by externally injected waves, it is better to separate the background fields from the time dependent wave fields. Moreover, since these fields vary much faster than the time scales of interest, a first time

average has been done, hence $f_e \longrightarrow \bar{f}_e$. It is here that the quasilinear operator $\mathcal{Q}(\bar{f}_e)$, which describes the effect of the external waves, has been introduced.

At this point, since charged particles undergo periodic motion around magnetic field lines, which occurs on time scale which are fast compared to the transit or the collision time scales, $\bar{f}_e$ is expanded in a small parameter, expressed as the ratio of the gyro and collision timescales. The zeroth order $\bar{f}_{e,0}$ is independent of the gyro angle, while the first order correction $\bar{f}_{e,1}$ is changing proportionally to the gyro motion timescale.

After this first ordering, an average over the gyro-angle is done to get rid of the electron motion around the field lines but keeping the main effects that this motion produces, hence $\bar{f}_{e,0} \longrightarrow \tilde{f}_{e,0}$. At this point, the dimensionality of the problem has been reduced, since the equation has been averaged over one full period of one of the angular coordinates. It is important to note that the gyro-averaged first-order equation does not depend on $\tilde{f}_{e,1}$.

As explained in Section 2.1, particles moving in a tokamak are drifting away from the magnetic field lines. The time scale of this phenomenon can vary, but in the small drift limit, it is much slower than the transit time. It is possible to expand again the distribution function, this time in δ_d, defined previously in Eq. (2.39). Once this step has been done, ordering the terms leads to the zeroth order Fokker-Plank equation when just considering the zeroth order terms, and to the drift-kinetic equation when considering the first order ones.

At this point the notation can be simplified, defining $\tilde{f}_{e,00} \equiv f_0$, and $\tilde{f}_{e,01} \equiv f_1$; we can now more easily proceed with the bounce-averaging. Looking to the time scale ordering (2.19), the next fastest time scale is the one associated with the transit or bounce time τ_b. In the low collisionality regime, electrons are assumed to be able to complete many poloidal transits before a collision could deflect them from their orbits, and hence the ratio $\delta_b = \tau_b/\tau_c \ll 1$. In order to bounce-average the equations, the following integration must be performed:

$$\langle \cdots \rangle_\theta = \frac{1}{\tau_b} \oint_{\Gamma_s} \cdots \frac{\mathrm{d}s}{|v_s|}, \tag{2.43}$$

where Γ_s is the path the particle is following to complete a full poloidal turn. Since, as explained in Section (2.1), some particles can be trapped into banana orbits, the integration in this case must take into account the velocity sign σ:

$$\langle \cdots \rangle_\theta = \frac{1}{2\tau_b} \sum_{\sigma=\pm 1} \int_{s_{min}}^{s_{max}} \cdots \frac{\mathrm{d}s}{|v_s|}, \tag{2.44}$$

where s_{min} and s_{max} are the s coordinates at the two bounce points, which coincide in the case of a passing orbit. The last two expressions can be combined into

$$\langle \cdots \rangle_\theta = \frac{1}{\tau_b} \left[\frac{1}{2} \sum_{\sigma=\pm 1} \right]_T \int_{s_{min}}^{s_{max}} \cdots \frac{\mathrm{d}s}{|v_s|}, \tag{2.45}$$

where the square brackets are indicating that the sum applies only in the case of trapped particles. Since it is the most general case, from now on Eq. (2.45) will represent the bounce-averaging operation.

2.4.5.1 Zeroth order equation

In the low collisionality regime, the dominant term of Eq. (2.41) is

$$v_s \frac{\partial f_0}{\partial s} = 0, \tag{2.46}$$

which implies that f_0 is constant along the field lines, and that the bounce-averaged steady-state zeroth order Fokker-Plank equation reads

$$\langle \mathcal{C}(f_0) \rangle_\theta + \langle \mathcal{Q}(f_0) \rangle_\theta + \langle \mathcal{E}(f_0) \rangle_\theta = 0. \tag{2.47}$$

2.4.5.2 First order equation

Concerning Eq. (2.42) in the low collisionality regime, the dominant term is instead

$$v_s \frac{\partial f_1}{\partial s} + (\boldsymbol{v_D} \cdot \boldsymbol{\nabla} \psi) \frac{\partial f_0}{\partial \psi} = 0, \tag{2.48}$$

and it is possible to write

$$f_1 = \tilde{f} + g, \tag{2.49}$$

where g is constant along the field lines. An expression for $\tilde{f}$ is obtained when substituting Eq. (2.49) inside Eq. (2.48):

$$\tilde{f} = -\int (\boldsymbol{v_D} \cdot \boldsymbol{\nabla} \psi) \frac{\partial f_0}{\partial \psi} \frac{\mathrm{d}s}{v_s} = -\int \frac{v_\parallel}{\Omega_e} I(\psi) \boldsymbol{B} \cdot \boldsymbol{\nabla} \left(\frac{v_\parallel}{B} \right) \frac{\mathrm{d}s}{v_s}, \tag{2.50}$$

where for the last equality Eq. (2.37) has been used. Solving the integral and substituting in f_1, it is possible to show that [6]

$$\left\langle v_s \frac{\partial f_1}{\partial s} \right\rangle_\theta = 0. \tag{2.51}$$

In addition, it can be demonstrated that

$$\left\langle (\boldsymbol{v_D} \cdot \boldsymbol{\nabla}\psi) \frac{\partial f_0}{\partial \psi} \right\rangle_\theta = 0, \tag{2.52}$$

which means that, similarly to the zeroth order case, the bounced-averaged steady-state drift-kinetic equation reads

$$\langle \mathcal{C}(f_1) \rangle_\theta + \langle \mathcal{Q}(f_1) \rangle_\theta + \langle \mathcal{E}(f_1) \rangle_\theta = 0, \tag{2.53}$$

using Eq. (2.49), and assuming the linearity of the collision operator, it is possible to get the equation for g

$$\langle \mathcal{C}(g) \rangle_\theta + \langle \mathcal{Q}(g) \rangle_\theta + \langle \mathcal{E}(g) \rangle_\theta = -\langle \mathcal{C}(\tilde{f}) \rangle_\theta - \langle \mathcal{Q}(\tilde{f}) \rangle_\theta - \langle \mathcal{E}(\tilde{f}) \rangle_\theta, \tag{2.54}$$

where $\tilde{f}$ is obtained from Eq. (2.50).

2.5 Flux representation

From the conservation of the total number of particles, the steady state zeroth order Fokker-Plank Equation (2.47) can be written in the general conservative form

$$\left\langle \sum_{\mathcal{O}} \boldsymbol{\nabla} \cdot \boldsymbol{\mathcal{S}}_{\mathcal{O}}(f_0) \right\rangle_\theta = \langle \boldsymbol{\nabla} \cdot \boldsymbol{\mathcal{S}}_{\mathcal{C}}(f_0) + \boldsymbol{\nabla} \cdot \boldsymbol{\mathcal{S}}_{\mathcal{E}}(f_0) + \boldsymbol{\nabla} \cdot \boldsymbol{\mathcal{S}}_{\mathcal{Q}}(f_0) \rangle_\theta = 0, \tag{2.55}$$

where each term refers to the divergence of flux of particles due to each operator $\mathcal{O}$. Each flux operator can be expressed in the general diffusive-convective form

$$\boldsymbol{\mathcal{S}}_{\mathcal{O}}(f_0) = -\boldsymbol{D}_{\mathcal{O}} \cdot \boldsymbol{\nabla} f_0 + \boldsymbol{F}_{\mathcal{O}} f_0, \tag{2.56}$$

with $\boldsymbol{D}_{\mathcal{O}}$ the diffusion tensor, and $\boldsymbol{F}_{\mathcal{O}}$ the convective vector in the phase space $\{\boldsymbol{X} = (\psi, \theta, \phi), \boldsymbol{P} = (p, \xi, \varphi)\}$. After the bounce-averaging in Section 2.4.5 the dimensionality of the problem has been reduced, and the only remaining coordinates at this point are the flux surface coordinate ψ, the particle momentum p, and the cosine of the pitch angle ξ_0. This means that

$$\boldsymbol{D}_{\mathcal{O}} = \begin{pmatrix} D_{\mathcal{O}_{\psi\psi}} & D_{\mathcal{O}_{\psi p}} & D_{\mathcal{O}_{\psi\xi}} \\ D_{\mathcal{O}_{p\psi}} & D_{\mathcal{O}_{pp}} & D_{\mathcal{O}_{p\xi}} \\ D_{\mathcal{O}_{\xi\psi}} & D_{\mathcal{O}_{\xi p}} & D_{\mathcal{O}_{\xi\xi}} \end{pmatrix}, \tag{2.57}$$

$$\boldsymbol{F}_{\mathcal{O}} = \begin{pmatrix} F_{\mathcal{O}_\psi} \\ F_{\mathcal{O}_p} \\ F_{\mathcal{O}_\xi} \end{pmatrix}, \tag{2.58}$$

and the reduced gradient in the (ψ, p, ξ_0) space is

$$\boldsymbol{\nabla} = \begin{pmatrix} \nabla_\psi = |\nabla\psi|\partial/\partial\psi \\ \nabla_p = \partial/\partial p \\ \nabla_{\xi_0} = -\dfrac{\sqrt{1-\xi_0^2}}{p}\partial/\partial\xi_0 \end{pmatrix}. \tag{2.59}$$

Therefore, for a general operator $\mathcal{O}$ only acting in momentum space, the fluxes along momentum and pitch angle take the form

$$\mathcal{S}_{\mathcal{O}_p}(f_0) = -D_{\mathcal{O}_{pp}}\frac{\partial f_0}{\partial p} + \frac{\sqrt{1-\xi_0^2}}{p}D_{\mathcal{O}_{p\xi}}\frac{\partial f_0}{\partial \xi_0} + F_{\mathcal{O}_p} f_0, \tag{2.60}$$

$$\mathcal{S}_{\mathcal{O}_\xi}(f_0) = -D_{\mathcal{O}_{\xi p}}\frac{\partial f_0}{\partial p} + \frac{\sqrt{1-\xi_0^2}}{p}D_{\mathcal{O}_{\xi\xi}}\frac{\partial f_0}{\partial \xi_0} + F_{\mathcal{O}_\xi} f_0; \tag{2.61}$$

while the divergence of Eq. (2.55), again acting only in momentum space, can be generally expressed as

$$\boldsymbol{\nabla}\cdot\boldsymbol{\mathcal{S}}_{\mathcal{O}_p} = \frac{1}{p^2}\frac{\partial}{\partial p}(p^2\mathcal{S}_{\mathcal{O}_p}) - \frac{1}{p}\frac{\partial}{\partial \xi}\left(\sqrt{1-\xi^2}\mathcal{S}_{\mathcal{O}_\xi}\right), \tag{2.62}$$

where $\boldsymbol{\mathcal{S}}_{\mathcal{O}_p} = (\mathcal{S}_{\mathcal{O}_p}, \mathcal{S}_{\mathcal{O}_\xi})$. Applying the bounce-averaged operator to Eq. (2.62), and using linearity:

$$\left\langle \boldsymbol{\nabla}\cdot\boldsymbol{\mathcal{S}}_{\mathcal{O}_p}\right\rangle_\theta = \left\langle \frac{1}{p^2}\frac{\partial}{\partial p}(p^2\mathcal{S}_{\mathcal{O}_p})\right\rangle_\theta - \left\langle \frac{1}{p}\frac{\partial}{\partial \xi}\left(\sqrt{1-\xi^2}\mathcal{S}_{\mathcal{O}_\xi}\right)\right\rangle_\theta. \tag{2.63}$$

The calculation to simplify these integrals is quite lengthy and it is carefully done in [6]; here only the result is stated:

$$\left\langle \boldsymbol{\nabla}\cdot\boldsymbol{\mathcal{S}}_{\mathcal{O}_p}\right\rangle_\theta = \frac{1}{p^2}\frac{\partial}{\partial p}(p^2\mathcal{S}^{(0)}_{\mathcal{O}_p}) - \frac{1}{p}\frac{1}{\lambda}\frac{\partial}{\partial \xi}\left(\sqrt{1-\xi^2}\lambda\mathcal{S}^{(0)}_{\mathcal{O}_{\xi_0}}\right), \tag{2.64}$$

where

$$S^{(0)}_{\mathcal{O}_p} = \left\langle \mathcal{S}_{\mathcal{O}_p}\right\rangle_\theta \tag{2.65}$$

and

$$S^{(0)}_{\mathcal{O}_{\xi_0}} = \sigma\left\langle \frac{\sigma\xi}{\sqrt{\Psi}\xi_0}\mathcal{S}_{\mathcal{O}_\xi}\right\rangle_\theta \tag{2.66}$$

are the bounce-averaged fluxes, and

$$\lambda = \frac{1}{\tilde{q}} \int_{\theta_{min}}^{\theta_{max}} \frac{\mathrm{d}\theta}{2\pi} \frac{1}{|\hat{\boldsymbol{\psi}} \cdot \hat{\boldsymbol{r}}|} \frac{r}{R_P} \frac{B}{B_P} \frac{\xi_0}{\xi} \tag{2.67}$$

is the normalized bounce time, with

$$\tilde{q} = \int_0^{2\pi} \frac{\mathrm{d}\theta}{2\pi} \frac{1}{|\hat{\boldsymbol{\psi}} \cdot \hat{\boldsymbol{r}}|} \frac{r}{R_P} \frac{B}{B_P}. \tag{2.68}$$

It is now of interest to compute the bounce-averaged expressions for the diffusion and convective coefficients. Since the distribution function is different depending on the chosen approximation, i.e. if the drift effects are taken into account or not, the two cases must be treated separately. From now on, in order to simplify the notation, the bounce averaged distribution function will be indicated as $f_0^{(0)}$.

2.5.1 Zeroth order equation

As stated in Eq. (2.46), f_0 is constant along the field lines, which means that $f_0(p,\xi) = f_0^{(0)}(p,\xi_0)$. Now, substituting Eqs. (2.60)-(2.61) into Eqs. (2.65)-(2.66):

$$\mathcal{S}^{(0)}_{\mathcal{O}_p}(f_0) = -D^{(0)}_{\mathcal{O}_{pp}} \frac{\partial f_0^{(0)}}{\partial p} + \frac{\sqrt{1-\xi_0^2}}{p} D^{(0)}_{\mathcal{O}_{p\xi_0}} \frac{\partial f_0^{(0)}}{\partial \xi_0} + F^{(0)}_{\mathcal{O}_p} f_0^{(0)}, \tag{2.69}$$

$$\mathcal{S}^{(0)}_{\mathcal{O}_{\xi_0}}(f_0) = -D^{(0)}_{\mathcal{O}_{\xi p}} \frac{\partial f_0^{(0)}}{\partial p} + \frac{\sqrt{1-\xi_0^2}}{p} D^{(0)}_{\mathcal{O}_{\xi\xi}} \frac{\partial f_0^{(0)}}{\partial \xi_0} + F^{(0)}_{\mathcal{O}_\xi} f_0^{(0)}, \tag{2.70}$$

where

$$D^{(0)}_{\mathcal{O}_{pp}} = \left\langle D_{\mathcal{O}_{pp}} \right\rangle_\theta , \tag{2.71}$$

$$D^{(0)}_{\mathcal{O}_{p\xi}} = \sigma \left\langle \frac{\sigma\xi}{\sqrt{\Psi}\xi_0} D_{\mathcal{O}_{p\xi}} \right\rangle_\theta , \tag{2.72}$$

$$D^{(0)}_{\mathcal{O}_{\xi p}} = \sigma \left\langle \frac{\sigma\xi}{\sqrt{\Psi}\xi_0} D_{\mathcal{O}_{\xi p}} \right\rangle_\theta , \tag{2.73}$$

$$D^{(0)}_{\mathcal{O}_{\xi\xi}} = \left\langle \frac{\xi^2}{\Psi\xi_0^2} D_{\mathcal{O}_{\xi\xi}} \right\rangle_\theta , \tag{2.74}$$

$$F^{(0)}_{\mathcal{O}_p} = \left\langle F_{\mathcal{O}_p} \right\rangle_\theta , \tag{2.75}$$

$$F^{(0)}_{\mathcal{O}_\xi} = \sigma \left\langle \frac{\sigma\xi}{\sqrt{\Psi}\xi_0} F_{\mathcal{O}_\xi} \right\rangle_\theta . \tag{2.76}$$

2.5.2 First order equation

In this case $f_1 = \tilde{f} + g$, where g is constant along the field lines, which means that the respective diffusion and convective coefficients can be computed exactly as it has been done with the coefficients of f_0. What differs now from the Fokker-Plank case is the $\tilde{f}$ term, which is dependent on the poloidal angle θ. The explicit dependence on θ can be isolated as

$$\tilde{f} = \frac{\xi}{\Psi\xi_0} \tilde{f}^{(0)}, \tag{2.77}$$

where

$$\tilde{f}^{(0)} = \frac{p\xi_0}{q} \frac{I}{B_0} \frac{\partial f_0^{(0)}}{\partial\psi}, \tag{2.78}$$

with ξ being the only variable dependent on θ, and $I = I(\psi) = B_T/|\boldsymbol{\nabla}\phi|$ as shown in Eq. (2.36). Here again, the full derivation of the bounce-averaged coefficients is quite lengthy and it can be found in [6]; below only the results are given:

$$\mathcal{S}^{(0)}_{\mathcal{O}_p}(\tilde{f}) = -\tilde{D}^{(0)}_{\mathcal{O}_{pp}} \frac{\partial\tilde{f}^{(0)}}{\partial p} + \frac{\sqrt{1-\xi_0^2}}{p} \tilde{D}^{(0)}_{\mathcal{O}_{p\xi}} \frac{\partial\tilde{f}^{(0)}}{\partial\xi_0} + \tilde{F}^{(0)}_{\mathcal{O}_p} \tilde{f}^{(0)}, \tag{2.79}$$

$$\mathcal{S}^{(0)}_{\mathcal{O}_{\xi_0}}(\tilde{f}) = -\tilde{D}^{(0)}_{\mathcal{O}_{\xi p}} \frac{\partial\tilde{f}^{(0)}}{\partial p} + \frac{\sqrt{1-\xi_0^2}}{p} \tilde{D}^{(0)}_{\mathcal{O}_{\xi\xi}} \frac{\partial\tilde{f}^{(0)}}{\partial\xi_0} + \tilde{F}^{(0)}_{\mathcal{O}_\xi} \tilde{f}^{(0)}, \tag{2.80}$$

where

$$\tilde{D}^{(0)}_{\mathcal{O}_{pp}} = \sigma \left\langle \frac{\sigma\xi}{\Psi\xi_0} D_{\mathcal{O}_{pp}} \right\rangle_\theta , \tag{2.81}$$

$$\tilde{D}^{(0)}_{\mathcal{O}_{p\xi}} = \left\langle \frac{\xi^2}{\Psi^{3/2}\xi_0^2} D_{\mathcal{O}_{p\xi}} \right\rangle_\theta , \tag{2.82}$$

$$\tilde{D}^{(0)}_{\mathcal{O}_{\xi p}} = \left\langle \frac{\xi^2}{\Psi^{3/2}\xi_0^2} D_{\mathcal{O}_{\xi p}} \right\rangle_\theta , \tag{2.83}$$

$$\tilde{D}^{(0)}_{\mathcal{O}_{\xi\xi}} = \sigma \left\langle \frac{\sigma\xi^3}{\Psi^2\xi_0^3} D_{\mathcal{O}_{\xi\xi}} \right\rangle_\theta , \tag{2.84}$$

$$\tilde{F}^{(0)}_{\mathcal{O}_p} = \sigma \left\langle \frac{\sigma\xi}{\Psi\xi_0} F_{\mathcal{O}_p} \right\rangle_\theta + \frac{\sqrt{1-\xi_0^2}}{p\xi_0^3} \left\langle \frac{(\Psi-1)}{\Psi^{3/2}} D_{\mathcal{O}_{p\xi}} \right\rangle_\theta , \tag{2.85}$$

$$\tilde{F}^{(0)}_{\mathcal{O}_\xi} = \left\langle \frac{\xi^2}{\Psi^{3/2}\xi_0^2} F_{\mathcal{O}_\xi} \right\rangle_\theta + \frac{\sqrt{1-\xi_0^2}}{p\xi_0^3} \sigma \left\langle \frac{\sigma\xi(\Psi-1)}{\xi_0\Psi^2} D_{\mathcal{O}_{\xi\xi}} \right\rangle_\theta . \tag{2.86}$$

2.5.3 Bounce coefficients

When bounce-averaging the momentum-space operators, the result can be written using a set of coefficients, denoted $\lambda_{k,l,m}$ and $\overline{\lambda}_{k,l,m}$, defined as [6]

$$\frac{\lambda_{k,l,m}(\psi,\xi_0)}{\lambda(\psi,\xi_0)} = \left\langle \left(\frac{\xi(\psi,\theta,\xi_0)}{\xi_0} \right)^k \Psi^l(\psi,\theta) \left(\frac{R_0(\psi)}{R(\psi,\theta)} \right)^m \right\rangle , \tag{2.87}$$

$$\frac{\overline{\lambda}_{k,l,m}(\psi,\xi_0)}{\lambda(\psi,\xi_0)} = \sigma \left\langle \sigma \left(\frac{\xi(\psi,\theta,\xi_0)}{\xi_0} \right)^k \Psi^l(\psi,\theta) \left(\frac{R_0(\psi)}{R(\psi,\theta)} \right)^m \right\rangle , \tag{2.88}$$

where $R_0(\psi) \equiv R(\psi,\theta_0)$ and

$$\overline{\lambda}_{k,l,m} = \begin{cases} \lambda_{k,l,m} & \text{for passing particles,} \\ 0 & \text{for trapped particles.} \end{cases} \tag{2.89}$$

2.6 The synchrotron reaction force

When a charged particle accelerates, it disrupts the surrounding electromagnetic field, causing perturbations that propagate through space as electromagnetic waves. The type of radiation emitted depends on the particle's speed relative to the speed of light. At non-relativistic speeds, the emitted radiation is known as cyclotron radiation. On the other hand,

when the particle's speed approaches that of light, the emitted radiation is called synchrotron radiation. As illustrated in Figure 2.5, another major characteristic of synchrotron radiation is that it is beamed into the forward direction of electron, due to relativistic effects.

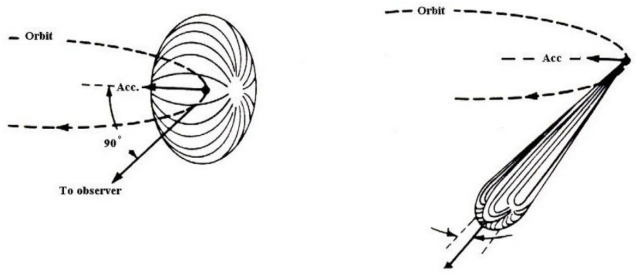

Figure 2.5: The shape of the emitted radiation in the case of cyclotron (left,low energy) and synchrotron (right, highly relativistic) emission [7].

In the context of plasma physics, particularly in tokamaks, synchrotron radiation serves a critical diagnostic function: it is especially useful for detecting runaway electrons as they gain sufficient energy to reach relativistic speeds. The synchrotron power emitted by a single electron can be generally expressed (in SI units) as [8]

$$P_{syn} = \frac{q^2}{6\pi\varepsilon_0 c^3}\gamma^6 \left[\left(\dot{\boldsymbol{v}} \cdot \frac{\boldsymbol{v}}{c} \right)^2 + \left(1 - \frac{v^2}{c^2} \right) |\dot{\boldsymbol{v}}|^2) \right], \tag{2.90}$$

where q is the electron charge, c is the speed of light and γ is the Lorentz factor.

Considering the expression for power in Eq. (2.90), it is clear that as electrons accelerate, they emit more synchrotron radiation. This increased radiation leads to a loss of energy, analogous to a frictional force acting on the electrons. Due to the conservation of energy, this "frictional" force means that runaway electrons cannot accelerate indefinitely. Instead, they eventually reach a steady state in their momentum.

This synchrotron reaction force is also known as the Abraham-Lorentz-Dirac (ALD) force $\boldsymbol{F}_{\text{ALD}}$, and it is responsible for the energy threshold reached by runaways electrons. The ALD force takes the general expression [9]

$$\boldsymbol{F}_{\text{ALD}} = \frac{q^2\gamma^2}{6\pi\epsilon_0 c^3} \left[\ddot{\boldsymbol{v}} + \frac{3\gamma^2}{c^2}(\boldsymbol{v}\cdot\dot{\boldsymbol{v}})\dot{\boldsymbol{v}} + \frac{\gamma^2}{c^2}\left(\boldsymbol{v}\cdot\ddot{\boldsymbol{v}} + \frac{3\gamma^2}{c^2}(\boldsymbol{v}\cdot\dot{\boldsymbol{v}})^2 \right)\boldsymbol{v} \right]. \tag{2.91}$$

In a uniform and constant magnetic field the ALD force reduces to [9]

$$\boldsymbol{F}_{\mathrm{ALD}} \simeq -\frac{m}{\tau_r}\left[\boldsymbol{v}_\perp + \frac{\gamma^2 v_\perp^2}{c^2}\boldsymbol{v}\right], \tag{2.92}$$

where

$$\tau_r = \frac{6\pi\varepsilon_0 (mc)^3}{e^4 B^2} \tag{2.93}$$

is the synchrotron radiation reaction timescale.

2.6.1 Synchrotron operator

In Eq. (2.13), the only force considered is the Lorentz force. When considering additional forces new operators can be obtained. This is the case for the synchrotron reaction force. Adding $\boldsymbol{F}_{\mathrm{ALD}}$ to the forces in Eq. (2.13), yields a new flux $\boldsymbol{\mathcal{S}}_{\mathcal{S}}(f_0)$ in the steady-state Fokker-Plank equation, Eq. (2.55). The momentum and pitch components of the flux are respectively

$$\mathcal{S}_{\mathcal{S}_p}(f_0) = F_{\mathcal{S}_p} f_0, \tag{2.94}$$

$$\mathcal{S}_{\mathcal{S}_\xi}(f_0) = F_{\mathcal{S}_\xi} f_0; \tag{2.95}$$

where

$$F_{\mathcal{S}_p} = -\frac{\gamma p(1-\xi^2)}{\tau_r}, \tag{2.96}$$

$$F_{\mathcal{S}_\xi} = -\frac{1}{\tau_r}\frac{p\xi\sqrt{1-\xi^2}}{\gamma}. \tag{2.97}$$

2.6.1.1 Zeroth order equation

Bounce averaging of the flux coefficients in Eqs. (2.96)-(2.97) can be done either in the zero orbit width approximation, Eqs. (2.75)-(2.76), or in the small orbit width approximation, Eqs. (2.85)-(2.86). The code LUKE was already equipped with the synchrotron force in the zeroth order approximation, and

the bounce averaged flux coefficients are here derived again:

$$\begin{aligned} F^{(0)}_{\mathcal{S}_p} &= \left\langle F_{\mathcal{S}_p} \right\rangle_\theta \\ &= \left\langle -\frac{\gamma p (1-\xi^2)}{\tau_r} \right\rangle_\theta \\ &= -\frac{p\gamma(1-\xi_0^2)}{\tilde{q}^2 \tau_{r,ref}} \frac{B_0^2}{B_{ref}^2} \left\langle \Psi^3 \right\rangle_\theta \\ &= -\frac{p\gamma(1-\xi_0^2)}{\tilde{q} \tau_{r,ref}} \frac{B_0^2}{B_{ref}^2} \frac{\lambda_{0,3,0}}{\lambda}, \end{aligned} \tag{2.98}$$

$$\begin{aligned} F^{(0)}_{\mathcal{S}_\xi} &= \sigma \left\langle \frac{\sigma\xi}{\sqrt{\Psi}\xi_0} F_{\mathcal{S}_\xi} \right\rangle_\theta \\ &= \sigma \left\langle -\frac{\sigma\xi}{\sqrt{\Psi}\xi_0} \frac{1}{\tau_r} \frac{p\xi\sqrt{1-\xi^2}}{\gamma} \right\rangle_\theta \\ &= -\frac{p\xi_0\sqrt{1-\xi_0^2}}{\tilde{q}\gamma\tau_{r,ref}} \frac{B_0^2}{B_{ref}^2} \left\langle \left(\frac{\xi}{\xi_0}\right)^2 \Psi^2 \right\rangle_\theta \\ &= -\frac{p\xi_0\sqrt{1-\xi_0^2}}{\tilde{q}\gamma\tau_{r,ref}} \frac{B_0^2}{B_{ref}^2} \frac{\lambda_{2,2,0}}{\lambda}, \end{aligned} \tag{2.99}$$

where the definition of the bounce coefficients in Eq. (2.87) has been used, and where $\tau_{r,ref}$ is the synchrotron radiation reaction timescale computed at a reference field B_{ref}.

2.6.1.2 First order equation

Before the work done in this thesis, the part of the code working with the small orbit width approximation, was not equipped with the synchrotron force, and the bounce averaged flux coefficients for this case are here derived for the first

time:

$$\begin{aligned}\tilde{F}^{(0)}_{\mathcal{S}_p} &= \sigma \left\langle \frac{\sigma\xi}{\Psi\xi_0} F_{\mathcal{S}_p} \right\rangle_\theta \\ &= \sigma \left\langle -\frac{\sigma\xi}{\Psi\xi_0} \frac{\gamma p(1-\xi^2)}{\tau_r} \right\rangle_\theta \\ &= -\frac{p\gamma(1-\xi_0^2)}{\tilde{q}\tau_{r,ref}} \frac{B_0^2}{B_{ref}^2} \sigma \left\langle \sigma \left(\frac{\xi}{\xi_0}\right) \Psi^2 \right\rangle_\theta \\ &= -\frac{p\gamma(1-\xi_0^2)}{\tilde{q}\tau_{r,ref}} \frac{B_0^2}{B_{ref}^2} \frac{\overline{\lambda}_{1,2,0}}{\lambda},\end{aligned} \tag{2.100}$$

$$\begin{aligned}\tilde{F}^{(0)}_{\mathcal{S}_\xi} &= \left\langle \frac{\xi^2}{\Psi^{3/2}\xi_0^2} \tilde{F}_{\mathcal{S}_\xi} \right\rangle_\theta \\ &= \left\langle -\frac{\xi^2}{\Psi^{3/2}\xi_0^2} \frac{1}{\tau_r} \frac{p\xi\sqrt{1-\xi^2}}{\gamma} \right\rangle_\theta \\ &= -\frac{p\xi_0\sqrt{1-\xi_0^2}}{\tilde{q}\gamma\tau_{r,ref}} \frac{B_0^2}{B_{ref}^2} \sigma \left\langle \sigma \left(\frac{\xi}{\xi_0}\right)^3 \Psi \right\rangle_\theta \\ &= -\frac{p\xi_0\sqrt{1-\xi_0^2}}{\tilde{q}\gamma\tau_{r,ref}} \frac{B_0^2}{B_{ref}^2} \frac{\overline{\lambda}_{3,1,0}}{\lambda},\end{aligned} \tag{2.101}$$

Having the synchrotron force also available in the first order calculation means that it is possible to run runaway simulations taking into account neoclassical effects as well.

2.6.2 Circular configuration

In the case of circular concentric flux surfaces, where $\psi = \psi(r)$ and $\hat{\boldsymbol{\psi}} = \hat{\boldsymbol{r}}$, the bounce coefficients defined in Eqs. (2.87)-(2.88) can be computed analytically. In particular, the bounce coefficients appearing in the synchrotron force flux, both in the zeroth and first order case, of Eqs. (2.98)-(2.99)-(2.100)-(2.101), have been derived here for the first time:

- Calculation of $\lambda_{1,2,0}$

$$\begin{aligned}\lambda_{1,2,0} &= \lambda \left\langle \frac{\xi}{\xi_0}\Psi^2 \right\rangle_\theta \\ &= \int_{-\theta_c}^{\theta_c} \frac{\mathrm{d}\theta}{2\pi}\frac{\xi_0}{\xi}\frac{\xi}{\xi_0}\Psi^2 \\ &= \frac{1}{\pi}\int_0^{\theta_c} \mathrm{d}\theta \Psi^2,\end{aligned} \tag{2.102}$$

where

$$\theta_c = \begin{cases} \pi & \text{for passing particles,} \\ \theta_T = \cos^{-1}(1 - 2\xi_0^2/\xi_{0T}^2) & \text{for trapped particles,} \end{cases} \tag{2.103}$$

with ξ_{0T} defined in Eq. (2.16). In the circular configuration, Ψ can be rewritten as [6]

$$\Psi(r,\theta) = \frac{1}{1 - \xi_{0T}^2 \sin^2(\alpha)}, \tag{2.104}$$

with $\alpha = \theta/2$. At this point $\lambda_{1,2,0}$ can be expressed as

$$\lambda_{1,2,0} = \frac{2}{\pi}\int_0^{\alpha_c} \mathrm{d}\alpha \frac{1}{\left[1 - \xi_{0T}^2 \sin^2(\alpha)\right]^2}, \tag{2.105}$$

and, using the geometric series

$$\frac{1}{1-x} = \sum_{n=0}^{\infty} x^n, \tag{2.106}$$

with $|x| < 1$, differentiating both sides

$$\frac{\mathrm{d}}{\mathrm{dx}}\left(\frac{1}{1-x}\right) = \frac{\mathrm{d}}{\mathrm{dx}}\left(\sum_{n=0}^{\infty} x^n\right) \longrightarrow \frac{1}{(1-x)^2} = \sum_{n=1}^{\infty} n x^{n-1}, \tag{2.107}$$

and taking $x = \xi_{0T}^2 \sin^2(\alpha)$, and $m = n - 1$, it is possible to rewrite Eq.

(2.105) as

$$\begin{aligned}\lambda_{1,2,0} &= \frac{2}{\pi}\sum_{m=0}^{\infty}(m+1)\int_0^{\alpha_c} \mathrm{d}\alpha\ x^m \\ &= \frac{2}{\pi}\sum_{m=0}^{\infty}(m+1)\xi_{0T}^{2m}\int_0^{\alpha_c} \mathrm{d}\alpha\ \sin^{2m}(\alpha) \\ &= \frac{2}{\pi}\sum_{m=0}^{\infty}(m+1)\xi_{0T}^{2m} Z_m,\end{aligned} \tag{2.108}$$

having defined

$$Z_m \equiv \int_0^{\alpha_c} \mathrm{d}\alpha\ \sin^{2m}(\alpha). \tag{2.109}$$

It is possible to demonstrate the following recursive relation, valid for every m:

$$Z_{m+1} = \frac{2m+1}{2m+2}Z_m - \frac{1}{2m+2}\cos(\alpha_c)\sin^{2m+1}(\alpha_c), \tag{2.110}$$

where $Z_0 = \alpha_c$.

For passing particles ($|\xi_0| > \xi_{0T}$) $\alpha_c = \pi/2$, therefore

$$Z_{m+1} = \frac{2m+1}{2m+2}Z_m; \tag{2.111}$$

for trapped particles ($|\xi_0| < \xi_{0T}$) instead, $\alpha_c = \theta_T/2$, hence

$$\sin\alpha_c = \sqrt{\frac{1-\cos\theta_T}{2}} = \frac{|\xi_0|}{\xi_{0T}}, \tag{2.112}$$

$$\cos\alpha_c = \sqrt{\frac{1+\cos\theta_T}{2}} = \frac{\sqrt{\xi_{0T}^2-\xi_0^2}}{\xi_{0T}}, \tag{2.113}$$

and

$$Z_{m+1} = \frac{2m+1}{2m+2}Z_m - \frac{\sqrt{\xi_{0T}^2-\xi_0^2}}{2m+2}\frac{|\xi_0|^{2m+1}}{\xi_{0T}^{2m+2}}. \tag{2.114}$$

- Calculation of $\lambda_{3,1,0}$

$$\begin{aligned}\lambda_{3,1,0} &= \lambda \left\langle \frac{\xi^3}{\xi_0^3}\Psi \right\rangle_\theta \\ &= \frac{\lambda}{\xi_0^2}\left\langle \frac{\xi}{\xi_0}\Psi\left[1-\Psi(1-\xi_0^2)\right]\right\rangle_\theta \\ &= \frac{\lambda}{\xi_0^2}\left[\left\langle \frac{\xi}{\xi_0}\Psi\right\rangle_\theta - \left\langle \frac{\xi}{\xi_0}\Psi^2\right\rangle_\theta (1-\xi_0^2)\right] \\ &= \frac{\lambda_{1,1,0}-(1-\xi_0^2)\lambda_{1,2,0}}{\xi_0^2}\end{aligned} \tag{2.115}$$

where $\lambda_{1,2,0}$ can be obtained with Eq. (2.108), and $\lambda_{1,1,0}$ has been derived in [6]:

$$\lambda_{1,1,0} = \sqrt{\frac{1+\epsilon}{1-\epsilon}}, \tag{2.116}$$

where ϵ is the inverse of the aspect ratio $\epsilon = r/R_p$.

- Calculation of $\lambda_{0,3,0}$

$$\begin{aligned}\lambda_{0,3,0} &= \lambda \left\langle \Psi^3 \right\rangle_\theta \\ &= \int_{-\theta_c}^{\theta_c} \frac{\mathrm{d}\theta}{2\pi}\frac{\xi_0}{\xi}\Psi^3 \\ &= \frac{1}{\pi}\int_0^{\theta_c} \mathrm{d}\theta \frac{\xi_0}{\sqrt{1-\Psi(1-\xi_0^2)}}\Psi^3,\end{aligned} \tag{2.117}$$

and, using again Eq. (2.104)

$$\lambda_{0,3,0} = \frac{2}{\pi}\int_0^{\alpha_c} \mathrm{d}\alpha \frac{1}{\sqrt{1-\xi_{0T}^2/\xi_0^2\sin^2(\alpha)}\left[1-\xi_{0T}^2\sin^2(\alpha)\right]^{5/2}}. \tag{2.118}$$

Starting with the geometric series

$$\sqrt{1-x} = \sum_{n=0}^{\infty}\chi_n x^n, \tag{2.119}$$

where

$$\chi_n = \frac{2n-3}{2n}\chi_{n-1}, \tag{2.120}$$

and $\chi_0 = 1$; differentiating both sides three times, and, adjusting the

coefficients:

$$\frac{1}{(1-x)^{5/2}} = \sum_{m=0}^{\infty} \chi''_m x^m, \tag{2.121}$$

where

$$\chi''_m = \frac{2m+3}{2m}\chi_{m-1}, \tag{2.122}$$

and $\chi''_0 = 1$. At this point $\lambda_{0,3,0}$ can be rewritten as

$$\lambda_{0,3,0} = \frac{2}{\pi}\sum_{m=0}^{\infty} \chi''_m \xi_{0T}^{2m} J_{2m} \tag{2.123}$$

where

$$J_{2m} = \int_0^{\alpha_c} \mathrm{d}\alpha \frac{\sin^{2m}(\alpha)}{\sqrt{1-\xi_{0T}^2/\xi_0^2 \sin^2(\alpha)}}. \tag{2.124}$$

These integrals can be expressed in terms of elliptic integrals, as shown in [6].

- Calculation of $\lambda_{2,2,0}$

$$\begin{aligned}
\lambda_{2,2,0} &= \lambda \left\langle \frac{\xi^2}{\xi_0^2}\Psi^2 \right\rangle_\theta \\
&= \frac{\lambda}{\xi_0^2}\left\langle \Psi^2\left[1-\Psi(1-\xi_0^2)\right]\right\rangle_\theta \\
&= \frac{\lambda}{\xi_0^2}\left[\left\langle\Psi^2\right\rangle_\theta - \left\langle\Psi^3\right\rangle_\theta (1-\xi_0^2)\right] \\
&= \frac{\lambda_{0,2,0} - (1-\xi_0^2)\lambda_{0,3,0}}{\xi_0^2}
\end{aligned}. \tag{2.125}$$

While $\lambda_{0,3,0}$ has been previously obtained (Eq. (2.123)), $\lambda_{0,2,0}$ needs to

be derived. Following the same approach used for $\lambda_{0,3,0}$:

$$\begin{aligned}\lambda_{0,2,0} &= \lambda \left\langle \Psi^2 \right\rangle_\theta \\ &= \int_{-\theta_c}^{\theta_c} \frac{\mathrm{d}\theta}{2\pi} \frac{\xi_0}{\xi} \Psi^2 \\ &= \frac{1}{\pi} \int_0^{\theta_c} \mathrm{d}\theta \frac{\xi_0}{\sqrt{1-\Psi(1-\xi_0^2)}} \Psi^2 \\ &= \frac{2}{\pi} \int_0^{\alpha_c} \mathrm{d}\alpha \frac{1}{\sqrt{1-\xi_{0T}^2/\xi_0^2 \sin^2(\alpha)} \left[1-\xi_{0T}^2 \sin^2(\alpha)\right]^{3/2}} \\ &= \frac{2}{\pi} \sum_{m=0}^{\infty} \chi'_m \xi_{0T}^{2m} J_{2m},\end{aligned} \tag{2.126}$$

where

$$\chi'_m = \frac{2m+1}{2m} \chi_{m-1}, \tag{2.127}$$

and $\chi'_0 = 1$. Therefore, $\lambda_{2,2,0}$ can be finally expressed as

$$\lambda_{2,2,0} = \frac{2}{\pi \xi_0^2} \sum_{m=0}^{\infty} \left[\chi'_m - (1-\xi_0^2)\chi''_m\right] \xi_{0T}^2 J_{2m}. \tag{2.128}$$

2.7 The bootstrap current

The bootstrap current is a self-generated, non-inductive current that originates from the gradients in particle pressure and temperature. The physics underlying its creation is complex and requires several steps to fully grasp how it is generated and sustained.

As previously explained in this chapter, particles can get trapped in the magnetic mirror formed by the magnetic field variation along a field line and, because of the vertical drift which particles experience, the orbit has a radial extent. Depending on the sign of the parallel velocity, particles can experience an outward or inward drift with respect to the flux surface, as shown in the left side of Figure 2.6. Due to radial density gradients in the plasma, the inner orbits are more populated than the outer ones, leading to an asymmetry in the distribution function, i.e. there are more ions moving with a negative parallel velocity, as shown on the right side of Figure 2.6, while there are more electrons with a positive parallel velocity.

For this reason a net current, named the banana current, is generated, and

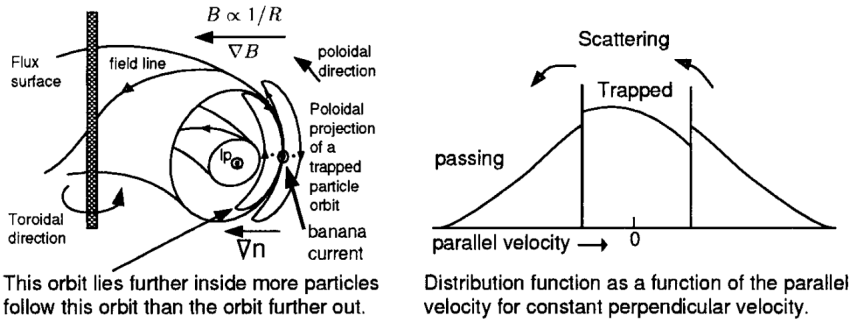

Figure 2.6: How the banana current is generated. On the left side different banana orbits are shown depending on the ion parallel velocity sign. On the right side the ion distribution affected by the density gradient is shown [10].

it can be easily estimated by multiplying the surplus of particles going in the current direction, their velocity, and their charge [10]:

$$J_B = \epsilon^{3/2} \frac{cT}{B_p} \frac{\partial n}{\partial r}, \tag{2.129}$$

where c is the speed of light and $\epsilon = r/R_p$ is the inverse aspect ratio.

This current only contributes to a fraction of the bootstrap current, which is mainly generated by passing particles subject to friction with trapped particles. This is because, when ions and electrons collide amongst themselves, their entire distributions get slightly shifted to the left for the ions and to the right for the electrons, as shown in Figure 2.7, due to the asymmetry in the trapped region*. This generates a difference in the fluid velocities, leading to the generation of the bootstrap current J_{BS}, which can be firstly estimated as [10]:

$$J_{BS} \approx \sqrt{\epsilon} \frac{cT}{B_p} \left[\frac{\mathrm{d}n_i}{\mathrm{d}r} + \frac{\mathrm{d}n_e}{\mathrm{d}r} \right]. \tag{2.130}$$

It is possible to note that $J_{BS}/J_B \approx 1/\epsilon \gg 1$, which indicates that the bootstrap current is significantly greater in magnitude than the banana current. Additionally, as particles move closer to the plasma center, they experience less variation in the magnetic field over a complete poloidal turn. Consequently, the region where particles are trapped becomes increasingly narrow, eventually vanishing at the center of the plasma. This causes the

*In reality, while ions mainly collide amongst themselves, since $\nu_{ii} \gg \nu_{ie}$, electrons mainly lose momentum through collisions with ions, since $\nu_{ei} \gg \nu_{ee}$, which means that their distribution function is less shifted than that of the ions.

bootstrap current to diminish and ultimately disappear at that point.

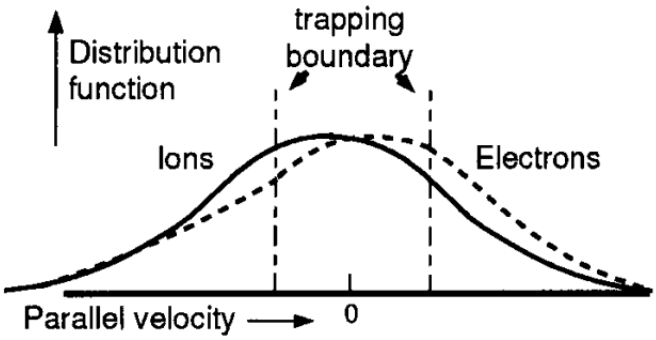

Figure 2.7: Asymmetry in the ion and electron distribution functions due to friction between trapped and passing particles [10].

In reality, the bootstrap current is also dependent on the temperature gradients, and it can generically be expressed as

$$\frac{\{\boldsymbol{J}_{BS}\cdot\boldsymbol{B}\}_\phi}{\{\boldsymbol{B}\cdot\boldsymbol{\nabla}\phi\}_\phi} = -\frac{p_e}{\{1/R^2\}_\phi}\left(\mathcal{L}_{31}A_1+\mathcal{L}_{32}A_2+\mathcal{L}_{34}A_4\right), \tag{2.131}$$

where $\{\cdots\}_\phi$ indicates the flux surface average, p_e the electron pressure and

$$A_1 = \frac{\mathrm{d\,ln\,p_e}}{\mathrm{d}\psi}+\frac{T_i}{Z_iT_e}\frac{\mathrm{d\,ln\,p_i}}{\mathrm{d}\psi}, \tag{2.132}$$

$$A_2 = \frac{\mathrm{d\,ln\,T_e}}{\mathrm{d}\psi}, \tag{2.133}$$

$$A_4 = \alpha_i\frac{T_i}{Z_iT_e}\frac{\mathrm{d\,ln\,T_i}}{\mathrm{d}\psi}, \tag{2.134}$$

with p_i and T_i the ion pressure and temperature, the transport coefficients $\mathcal{L}_{31}$, $\mathcal{L}_{32}$, $\mathcal{L}_{34}$, and the factor α_i depending on the model.

Chapter 3

Methods

3.1 LUKE: a bounce-averaged drift-kinetic Fokker-Plank solver

The code LUKE solves the linearized electron drift-kinetic equation for the electron distribution function f_e, in the plasma region where the weak collision banana regime holds [6]. In Chapter 2 the theory on which the code relies has been presented. Both the zeroth and the first order equations, respectively Eqs. (2.47) and (2.54), are solved; moments of the distribution function can be computed in both cases.

3.1.1 Grid definition

The code is solving the problem on the 3D volume (ψ, p, ξ_0), where the time evolution is considered when adding the variable t. The numerical method chosen to discretize Eqs. (2.47) and (2.54) is the finite difference method, and in [6] this procedure is carefully done. Since the equations are expressed in their conservative form, the grid is defined with the fluxes S being the starting point of the numerical calculations. This means that

$$S(t_k, \psi_l, p_i, \xi_{0,j}) \rightarrow \begin{cases} t_k \in [0, +\infty], & k \rightarrow \{0, n_t\} \\ \psi_l \in [0, \psi_a], & l \rightarrow \{0, n_\psi\} \\ p_i \in [0, p_{max}], & i \rightarrow \{0, n_p\} \\ \xi_{0,j} \in [-1, 1], & j \rightarrow \{0, n_{\xi_0}\} \end{cases} \tag{3.1}$$

while the distribution function is computed in the middle of each cell:

$$f(t_k, \psi_{l+1/2}, p_{i+1/2}, \xi_{0,j+1/2}) \rightarrow \begin{cases} t_k \in [0, +\infty], & k \rightarrow \{0, n_t\} \\ \psi_{l+1/2} \in \left[\frac{\Delta\psi_{1/2}}{2}, \psi_a - \frac{\Delta\psi_{n_\psi - 1/2}}{2}\right], & l \rightarrow \{0, n_\psi - 1\} \\ p_{i+1/2} \in \left[\frac{\Delta p_{1/2}}{2}, p_{max} - \frac{\Delta p_{n_p - 1/2}}{2}\right], & i \rightarrow \{0, n_p - 1\} \\ \xi_{0,j+1/2} \in \left[-1 + \frac{\Delta\xi_{0,1/2}}{2}, 1 - \frac{\Delta\xi_{0,n_{\xi,0}-1/2}}{2}\right], & j \rightarrow \{0, n_{\xi_0} - 1\} \end{cases} \tag{3.2}$$

This is shown in Figure 3.1, where the value of f in the middle of the cell is computed starting from the value of the fluxes going in and out of the same cell. In order to picture the spacial grid as well, it is sufficient to imagine the grid in Figure 3.1, replicated at every ψ_l. Concerning the time grid, the time step is taken always as uniform, hence $t_k = k\Delta t$.

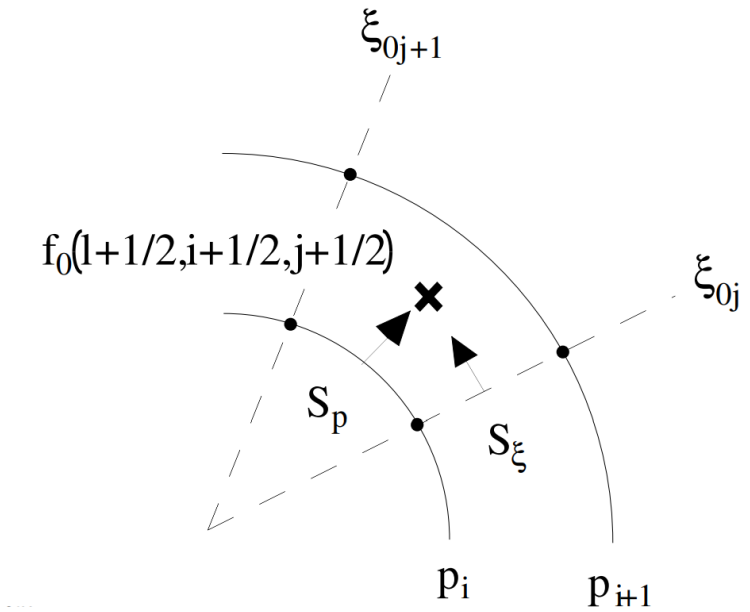

Figure 3.1: How the momentum grid is discretised in LUKE [6].

3.1.2 Distribution functions

Once the plasma conditions are selected and the grid is established, the code is capable of computing the electron distribution function across every point on the space and momentum grid. The zeroth order calculations, which solve Eq. (2.47) with operators tailored to the specific plasma conditions, yield

only the distribution f_0. In Figure 3.2, a contour of f_0, obtained solely using the collision operator, is depicted. Notably, this distribution is a Maxwellian centered at zero, which is consistent with expectations when only particle collisions are considered.

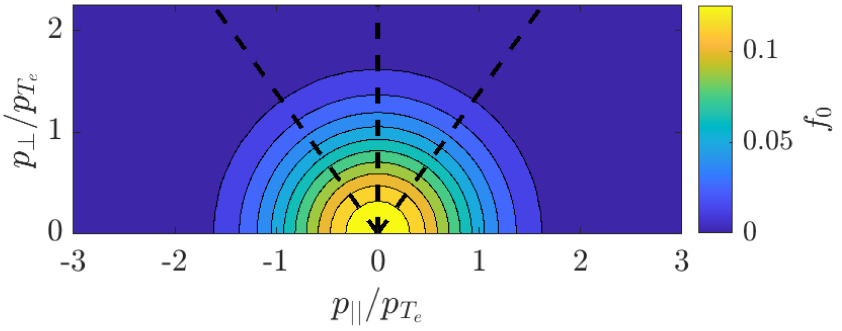

Figure 3.2: Example of f_0 distribution at $\psi_n = 0.5$. The dashed lines represent the trapped region.

The introduction of first order simulations, which were previously unavailable before the advancements made in this thesis, allows for the calculation of the distribution functions $\tilde{f}$ and g. The distribution $\tilde{f}$ is derived directly from f_0 using Eq. (2.50), while g is determined by solving Eq. (2.54). In Figures 3.3 and 3.4, examples of $\tilde{f}$ and g are illustrated under the same plasma conditions.

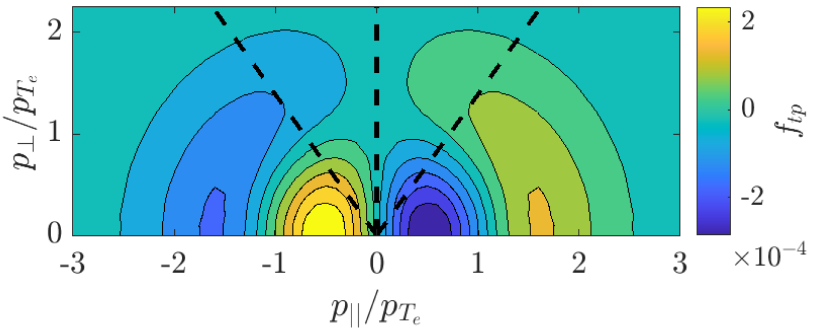

Figure 3.3: Example of $\tilde{f}$ distribution at $\psi_n = 0.5$. The dashed lines represent the trapped region.

It is interesting to observe that $\tilde{f}$ and g exhibit opposite signs, and that g is zero in the trapped region. Moreover, their combined effect, f_1, displayed

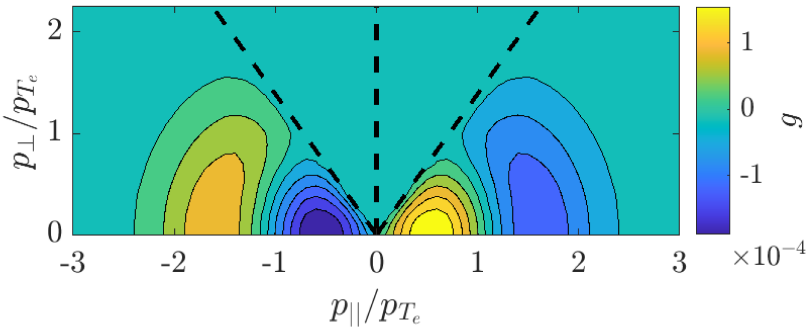

Figure 3.4: Example of g distribution at $\psi_n = 0.5$. The dashed lines represent the trapped region.

in Figure 3.5, is more than two orders of magnitude smaller than f_0. This indicates that although f_1 constitutes a minor correction to f_0, it is crucial for capturing neoclassical effects that would otherwise be overlooked.

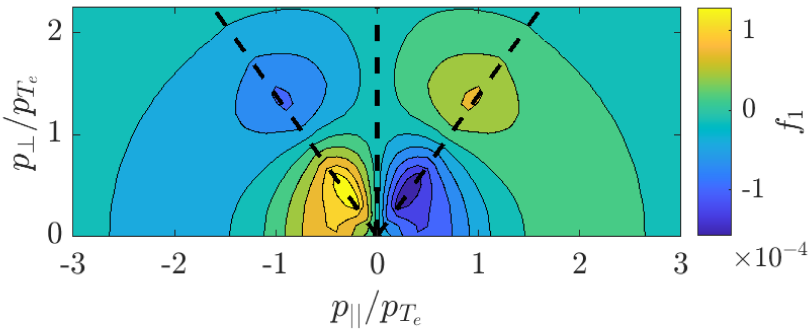

Figure 3.5: Example of f_1 distribution at $\psi_n = 0.5$. The dashed lines represent the trapped region.

3.2 Bootstrap current models

As outlined earlier, the existence of the bootstrap current is closely tied to the presence of trapped particles. If the collisionality of the plasma was too high, these trapped particles would scatter into the passing region before they could complete their banana orbits. This would eliminate the asymmetry in the distribution function that generates the bootstrap current. As a result, some

models of the bootstrap current assume a collisionless environment, where the collision timescale between trapped and passing particles is significantly longer than other relevant timescales, while others are derived in a general collisionality regime. Nevertheless, a minimal level of interaction must occur for the bootstrap current to be generated.

3.2.1 Hirshman model

The Hirshman model taken into account is considering one single species of ion with charge Z_i, in a collisionless plasma. Moreover, this model has been derived for arbitrary aspect ratio. In this case the previously defined coefficients take the form [11]

$$\mathcal{L}_{31} = x(0.754 + 2.21Z_i + Z_i^2) + x^2(0.347 + 1.24Z_i + Z_i^2)/D_e, \tag{3.3}$$

$$\mathcal{L}_{32} = -x(0.885 + 2.08Z_i)/D_e, \tag{3.4}$$

$$\mathcal{L}_{34} = \mathcal{L}_{31}, \tag{3.5}$$

$$\alpha_i = -\frac{1.17}{1.0 + 0.46x}, \tag{3.6}$$

$$\begin{aligned} D_e =& 1.41Z_i + Z_i^2 + x(0.754 + 2.65Z_i + 2.00Z_i^2) + \\ &+ x^2(0.347 + 1.24Z_i + Z_i^2), \end{aligned} \tag{3.7}$$

with $x = f_t/(1 - f_t)$ the ratio of trapped to circulating particles, which, in the limit of $\epsilon \ll 1$ can be obtained as

$$x = 1 - \frac{(1-\epsilon)^2}{\sqrt{1-\epsilon^2}(1 + 1.46\sqrt{\epsilon})}. \tag{3.8}$$

3.2.2 Hinton model

This model, which is the oldest of the ones presented here, has been derived by Hinton and Hazeltine in [12], in the case of arbitrary collisionality regime. The coefficients have been obtained by interpolation between the two limits $\epsilon = 0$ and $\epsilon = 1$, and the model performs better for large aspect ratios. Moreover, the contribution from the ions is separated from the one of the electrons. Even if the model can be used in different collsionality regimes, in this case the collisionless case is considered in order to compare it with the results from LUKE. The transport coefficients are functions of Z_i and x just for the ion

part. This means that instead of A_1 the model uses

$$A_{1,e} = \frac{\mathrm{d}\ln \mathrm{n_e}}{\mathrm{d}\psi}, \tag{3.9}$$

$$A_{1,i} = \frac{T_i}{Z_i T_e}\frac{\mathrm{d}\ln \mathrm{p_i}}{\mathrm{d}\psi}, \tag{3.10}$$

while A_2 and A_4 are the same as in Eqs.(2.133)-(2.134). The bootstrap current fraction generated by the electrons is then

$$\frac{\{\boldsymbol{J}_{BS,e}\cdot\boldsymbol{B}\}_\phi}{\{\boldsymbol{B}\cdot\boldsymbol{\nabla}\phi\}_\phi} = -\frac{p_e}{\{1/R^2\}_\phi}\left(2.44A_{1,e} + 0.69A_2\right), \tag{3.11}$$

while the fraction generated by ions is

$$\frac{\{\boldsymbol{J}_{BS,i}\cdot\boldsymbol{B}\}_\phi}{\{\boldsymbol{B}\cdot\boldsymbol{\nabla}\phi\}_\phi} = -\frac{p_e}{\{1/R^2\}_\phi}\left(\mathcal{L}_{31}A_{1,i} + \mathcal{L}_{34}A_4\right), \tag{3.12}$$

where $\mathcal{L}_{31}$ and $\mathcal{L}_{34}$ are computed exactly like in the Hirshman model (Eqs.(3.3)-(3.5)). The total bootstrap current is then obtained as

$$\{\boldsymbol{J}_{BS}\cdot\boldsymbol{B}\}_\phi = \{\boldsymbol{J}_{BS,e}\cdot\boldsymbol{B}\}_\phi + \{\boldsymbol{J}_{BS,i}\cdot\boldsymbol{B}\}_\phi. \tag{3.13}$$

3.2.3 Sauter model

This model is the most recent of the ones here presented. It has been obtained through fits from a Fokker-Planck solver coupled with the adjoint formalism. The model is more general, with the possibility of being used in arbitrary equilibrium and collisionality regimes. Here again, since the code LUKE operates at low plasma collisionality, just the collisionless case is presented.

The coefficients in this case are [13]:

$$\mathcal{L}_{31} = \left(1 + \frac{1.4}{Z_i + 1}\right) x - \frac{1.9}{Z_i + 1} x^2 + \frac{0.3}{Z_i + 1} x^3 + \frac{0.2}{Z_i + 1} x^4, \tag{3.14}$$

$$\begin{aligned}\mathcal{L}_{32} = &- \frac{0.51 + 1.31 Z_i}{Z_i (1 + 0.44 Z_i)} (x - x^4) + \frac{5.95 + 3.57 Z_i}{1 + 2.70 Z_i + 0.546 Z_i^2} (x^2 - x^4) + \\ &- \frac{3.92 + 3.57 Z_i}{1 + 2.70 Z_i + 0.546 Z_i^2} (x^3 - x^4),\end{aligned} \tag{3.15}$$

$$\mathcal{L}_{34} = \mathcal{L}_{31}, \tag{3.16}$$

$$\alpha_i = - \frac{1.17}{1.0 + 0.78 x - 0.19 \frac{x^2}{1+x}}, \tag{3.17}$$

where x is obtained as in Eq.(3.8).

Chapter 4

Results

4.1 Bootstrap current in LUKE

In order to get the bootstrap current radial profile from LUKE, it is sufficient to set all the parameters that characterize the plasma, choose temperature and pressure profiles for both ions and electrons, and run a simulation only taking into account collisions, i.e. without the electric field and wave operators. The profiles of temperature and pressure can be generally assumed as

$$T(\psi) = (T_0 - T_a)(1 - \psi^{b_T})^{a_T} + T_a, \tag{4.1}$$

$$p(\psi) = (p_0 - p_a)(1 - \psi^{b_p})^{a_p} + p_a, \tag{4.2}$$

for both ions and electrons, where $T_0 = T(\psi = 0)$, $T_a = T(\psi(a))$, $p_0 = p(\psi = 0)$ and $p_a = p(\psi(a))$, while b_T, a_T, b_p and a_p are coefficients used to adjust the profiles of temperature and pressure. The density profile can be immediately obtained as

$$n = \frac{p}{T}. \tag{4.3}$$

By differentiating these profiles, it is possible to calculate theoretical bootstrap currents for each LUKE simulation and compare them with the results obtained. Figures 4.1 illustrates some examples with varying profiles, and Table 4.1 summarizes the main parameters.

When examining the comparative analysis between the theoretical models and the results provided by LUKE, there is a noticeable alignment, especially highlighted in Figures 4.1a-4.1b. In the first case, the Sauter agrees better to the result obtained from the simulation; in the second scenario, the outcomes from the Sauter, Hirshmann, and LUKE models are remarkably consistent.

More broadly, the Hinton model appears to overestimate the bootstrap

Table 4.1: Summary of bootstrap current results presented in figures. The pressure is expressed in [10^{-19} keV/m^3] while the temperature is in [keV].

Figure	p_0	p_a	a_p	b_p	T_0	T_a	a_T	b_T	Z_i
Figure 4.1a	6.0	0.25	6	6	3	0.5	6	6	1
Figure 4.2a	6.0	0.25	6	1	3	0.5	6	1	1
Figure 4.1b	6.0	0.25	1	6	3	0.5	1	6	1
Figure 4.2b	6.0	0.25	6	6	3	0.5	1	1	1

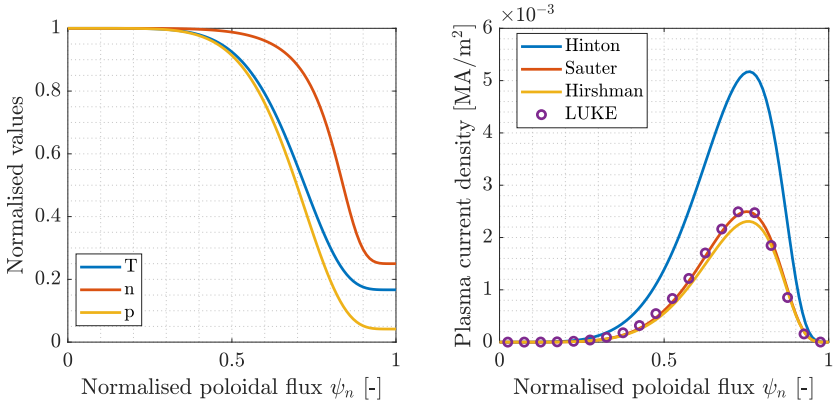

(a)

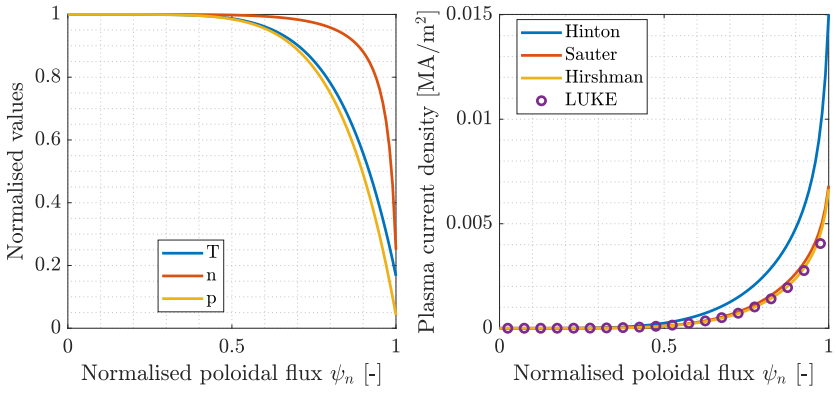

(b)

Figure 4.1: Bootstrap current profiles with different plasma characteristics. In Table 4.1 details regarding some plasma parameters are provided.

current across various scenarios. In Figure 4.2a, however, the LUKE result closely follows the trend predicted by the Hinton model, but diverges near the plasma center. At this central point, the current is theoretically, and according to the LUKE simulation, expected to decrease significantly, yet the Hinton

model does not capture this phenomenon.

Furthermore, Figure 4.2b introduces an exotic density profile to test the robustness and adaptability of computational approaches to unusual plasma conditions. In this case, while no model perfectly aligns with the LUKE results, the simulation still broadly mirrors them.

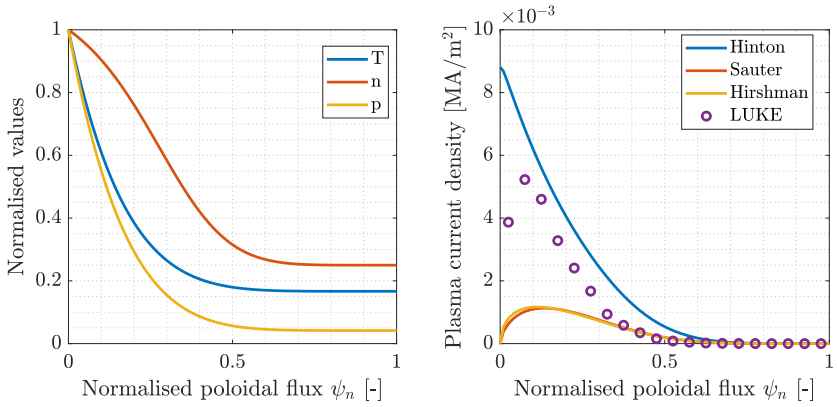

(a)

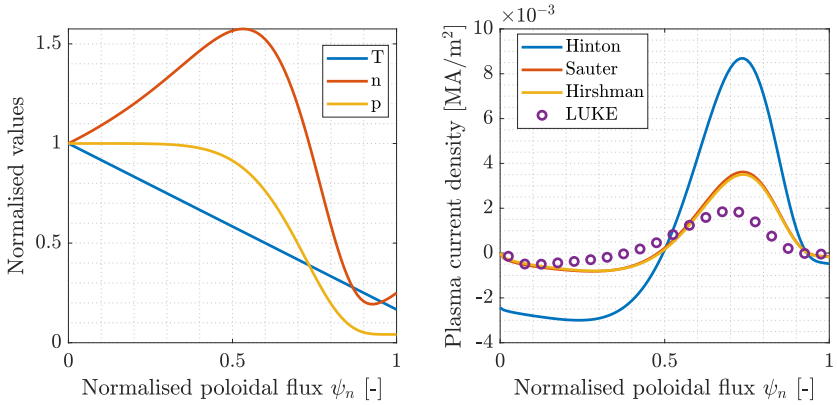

(b)

Figure 4.2: Bootstrap current profiles with different plasma characteristics. In Table 4.1 details regarding some plasma parameters are provided.

The results from the simulations using LUKE suggest that the bootstrap current calculations are fully restored, which is a promising development. However, it would be prudent to conduct a more extensive comparison with existing models across a variety of plasma scenarios to validate these findings further. As LUKE is a kinetic code that solves the drift-kinetic equation directly, it offers a highly general solution. This capability means that bootstrap current calculations can potentially be performed routinely after each

experimental discharge in various tokamaks, overcoming the limitations often associated with other models. This approach could lead to more accurate and consistent understanding of the bootstrap current in tokamak plasmas.

4.2 The effect of ALD force on runaways

After fully integrating the synchrotron operator into LUKE, it is now possible to analyze the behavior of runaway electrons, both with and without synchrotron effects, in the case of first order calculations. Previously, the code could account for synchrotron forces assuming a zero orbit width, a scenario extensively analyzed in [9]. By applying the same plasma conditions outlined in [9], it is possible to show the impact of the synchrotron force on the runaway electron population.

The density profiles for both ions and electrons are constant in the radial direction, specifically at $n_0 = 2{\cdot}10^{19}$ m^{-3}. The same holds for the temperature, where $T_0 = 5.11$ keV.

In Figures 4.3a-4.3b, the electron distribution function at $\psi_n = 0.5$ along the momentum parallel direction ($\xi = 1$) is presented. Figure 4.3a shows electrons accelerating until they exit the momentum domain, whereas Figure 4.3b illustrates the formation of a bump in the distribution tail, leading to a steady state where electrons cannot accelerate beyond a certain momentum threshold. The bump energy and magnitude, in relation to various plasma parameters, are analyzed in [9].

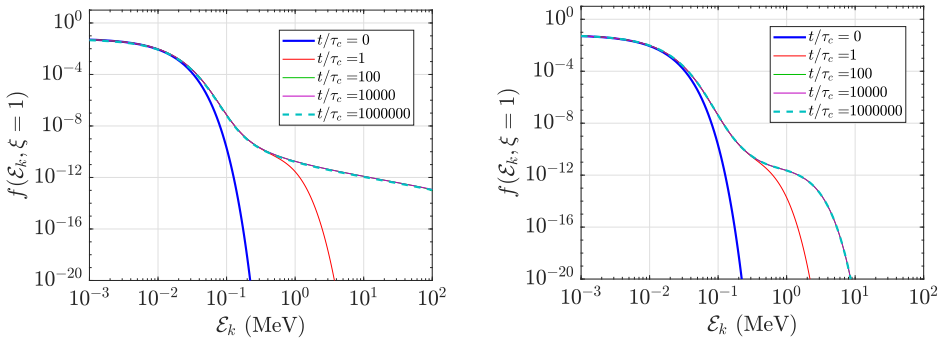

(a) Without ALD force.

(b) With ALD force.

Figure 4.3: Evolution of the electron distribution function in the zeroth order approximation as a function of the electron kinetic energy $\mathcal{E}_k$

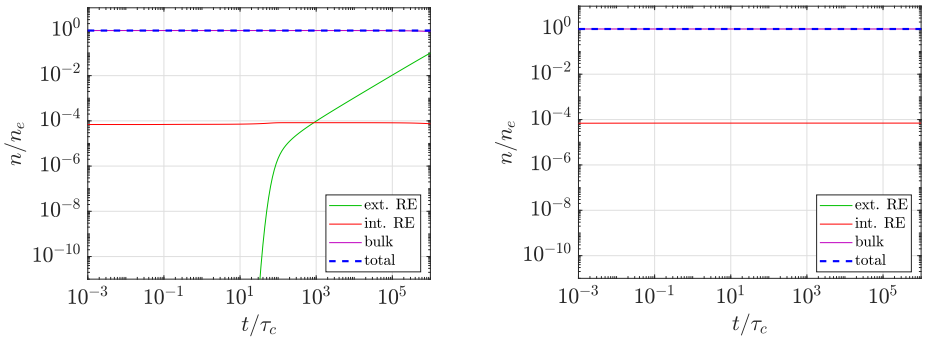

(a) Without ALD force.

(b) With ALD force.

Figure 4.4: Evolution of the runaway electron fraction outside and inside the simulation domain as a function of time normalized with respect the collision timescale τ_c.

Given the simulation's unbounded momentum domain, runaways that exceed the momentum limit are no longer simulated, leading to their removal from the domain. To maintain particle conservation, a source term based on the Maxwellian distribution at the local temperature is added at each grid point. Consequently, in scenarios without the ALD force, the electron distribution appears to stabilize, although this is not actually the case. This is evident in Figure 4.4a, where the fraction of external runaways increases significantly over time. In contrast, Figure 4.4b shows that, with the ALD force, runaways are generated but do not reach the domain boundary, preventing the generation of external runaways. The internal and external generation rates, which represents how much runaways are produced per second and per unit of volume, are shown in Figure 4.5. When not considering the ALD force, the internal runaway rate immediately drops as electrons reach the momentum boundary, while the external runaway rate suddenly increases, leading to a total runaway generation rate which is approximately constant. When considering ALD force, instead, the total runaway generation rate is only due to internal runaways, since they never reach the momentum boundary.

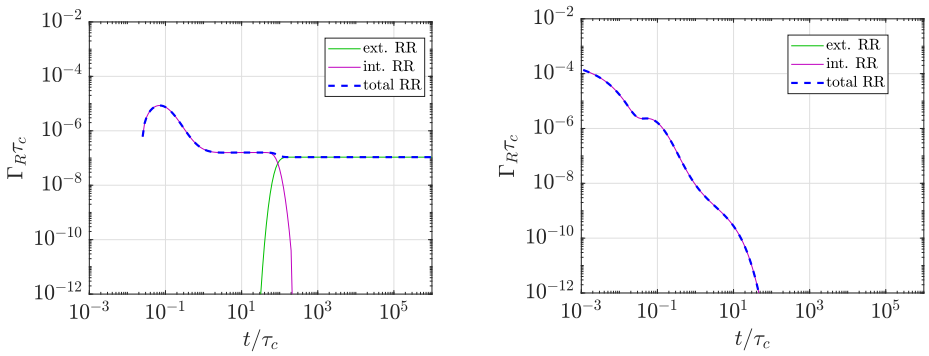

(a) Without ALD force.

(b) With ALD force.

Figure 4.5: Evolution of the runaway electron rates outside and inside the simulation domain as a function of time normalized with respect the collision timescale τ_c.

Chapter 5

Conclusions and Future work

This thesis has successfully addressed the challenge of restoring and enhancing the LUKE code's capability to accurately compute the bootstrap current in various plasma scenarios. By repairing and updating the LUKE code, it is now possible to calculate the bootstrap current: the comparison of LUKE's outputs with various theoretical models under different plasma conditions has demonstrated the solver's robustness and accuracy, thereby validating the implemented updates. Specifically, the bootstrap currents computed by LUKE align more closely with the Sauter and Hirshmann models, while the Hinton model tends to overestimate the bootstrap current. Since the results provided by LUKE are derived from solving the actual Fokker-Planck equation, this model is the most general, capable of calculating the bootstrap current in plasma conditions where analytical models might fail.

Furthermore, this thesis has expanded LUKE's scope by incorporating the neoclassical first-order synchrotron reaction force into its computational framework. The derivation and implementation of the synchrotron reaction force operator for neoclassical calculations have been done for the first time during this work. Although LUKE already included the synchrotron operator for zeroth-order calculations, enabling accurate simulation of runaway electrons in that case, it previously could not address finite orbit width cases. The first and zeroth-order synchrotron operators differ only in their bounce coefficients, which have also been analytically derived for circular configurations. Notably, the zeroth-order synchrotron operators are non-zero for trapped particles, which are affected by the ALD force irrespective of their velocity sign. Conversely, the first-order synchrotron operators have no net effect on trapped particles, as the respective bounce coefficients are zero in that case.

This advancement allows for more comprehensive simulations that include the effects of runaway electrons, which were previously not possible. The ability to simulate these effects within the neoclassical framework paves the way for future studies that could explore the complex interactions between runaway electrons and bootstrap currents in fusion plasmas.

Looking ahead, the groundwork laid by this thesis offers numerous pathways for further research. Future work should focus on developing simulations that specifically target the interplay between runaway electrons and the bootstrap current, aiming to provide a comprehensive understanding of the effect that runaway electrons may have on the bootstrap current. This could mean being able to compute the actual current carried by runaways; determining it experimentally is usually hard and not accurate, and, having a tool for that, would be a step forward in the runaway electrons study.

References

[1] N. C. for Environmental Information, "Monthly global climate report for annual 2023," *NOAA*, published online January 2024, retrieved on October 31, 2024. [Pages xiii and 1.]

[2] C. Ham, A. Kirk, S. Pamela, and H. Wilson, "Filamentary plasma eruptions and their control on the route to fusion energy," *Nature Reviews Physics*, vol. 2, no. 3, pp. 159–167, Mar 2020. doi: 10.1038/s42254-019-0144-1. [Online]. Available: https://doi.org/10.1038/s42254-019-0144-1 [Pages xiii and 3.]

[3] T. P. Kiviniemi, A. J. Virtanen, H. Systä, L. Chôné, S. Leerink, and E. Hirvijoki, "Simulating the effect of poloidal particle source on the bootstrap current and benchmarking to analytic estimates in tokamak edge pedestal," *Plasma Physics and Controlled Fusion*, vol. 63, no. 12, p. 125002, oct 2021. doi: 10.1088/1361-6587/ac2616. [Online]. Available: https://dx.doi.org/10.1088/1361-6587/ac2616 [Page 3.]

[4] M. Hoppe, "Runaway-electron model development and validation in tokamaks," Ph.D. dissertation, Department of Physics, Chalmers University of Technology, Göteborg, Sweden, 2021. [Pages xiii, 6, 8, and 11.]

[5] J. P. Freidberg, *Plasma Physics and Fusion Energy*. Cambridge University Press, 2007. [Page 6.]

[6] J. Decker and Y. Peysson, *LUKE: a fast numerical solver for the 3-D relativistic bounce-averaged electron Drift Kinetic Equation*. Association EURATOM-CEA sur la Fusion, 2019. [Pages xiii, 10, 12, 14, 17, 19, 21, 22, 27, 29, 30, 35, and 36.]

[7] [Online]. Available: https://commons.wikimedia.org/wiki/File:Synchrotron_radiation_energy_flux.png [Pages xiii and 23.]

[8] F. Shu, *The Physics of Astrophysics: Radiation*, ser. Series of books in astronomy. University Science Books, 1991. ISBN 9780935702644 [Page 23.]

[9] J. Decker, E. Hirvijoki, O. Embreus, Y. Peysson, A. Stahl, I. Pusztai, and T. Fulop, "Numerical characterization of bump formation in the runaway electron tail," Bristol, 2016. [Online]. Available: https://doi.org/10.1088/0741-3335/58/2/025016 [Pages 23, 24, and 46.]

[10] A. G. Peeters, "The bootstrap current and its consequences," *Plasma Physics and Controlled Fusion*, vol. 42, no. 12B, p. B231, dec 2000. doi: 10.1088/0741-3335/42/12B/318. [Online]. Available: https://dx.doi.org/10.1088/0741-3335/42/12B/318 [Pages xiii, 32, and 33.]

[11] C. Kessel, "Bootstrap current in a tokamak," *Nuclear Fusion*, vol. 34, no. 9, p. 1221, sep 1994. doi: 10.1088/0029-5515/34/9/I04. [Online]. Available: https://dx.doi.org/10.1088/0029-5515/34/9/I04 [Page 39.]

[12] F. L. Hinton and R. D. Hazeltine, "Theory of plasma transport in toroidal confinement systems," *Rev. Mod. Phys.*, vol. 48, pp. 239–308, Apr 1976. doi: 10.1103/RevModPhys.48.239. [Online]. Available: https://doi.org/10.1103/RevModPhys.48.239 [Page 39.]

[13] O. Sauter, C. Angioni, and Y. Lin-Liu, "Neoclassical conductivity and bootstrap current formulas for general axisymmetric equilibria and arbitrary collisionality regime," *Physics of Plasmas*, vol. 6, 07 1999. doi: 10.1063/1.873240 [Page 41.]